Energy Conversion and Management: X 28 (2025) 101316

Contents lists available at ScienceDirect

Energy Conversion and Management: X

journal homepage: www.sciencedirect.com/journal/energy-conversion-and-management-x

Artificial neural network-based power management for hybrid microgrid with SoC-supervised storage and dual-mode grid operation

Md. Badoruzzaman [a], Jahidul Islam Shuvo [a], Shaikh Tawhidul Islam Anik [a], Shameem Ahmad [b], A.S. Nazmul Huda [b], Tofael Ahmed [c], Mazaher Karimi [d,*]

[a] Department of Electrical and Electronic Engineering, American International University-Bangladesh, Dhaka 1229, Bangladesh
[b] Department of Electrical and Electronic Engineering, BSRM School of Engineering, BRAC University, Dhaka 1212, Bangladesh
[c] Department of Electrical and Electronic Engineering, Chittagong University of Engineering & Technology, Chattogram 4349, Bangladesh
[d] School of Technology and Innovations, University of Vaasa, Vaasa FI-65200, Finland

ARTICLE INFO

Keywords:
Hybrid energy storage
Energy management strategy
State-of-charge control
Microgrid
Grid Connected
ANN

ABSTRACT

Hybrid microgrids (HMGs) in grid-interactive settings historically relied on single-source generation or single-storage control that faltered under renewable intermittency, fast transients, and storage aging, constraining reliability and autonomy. This study developed a lightweight power-management system that coordinated solar photovoltaics (PV), wind, battery–supercapacitor (SC) storage, the utility grid, and AC load and electric-vehicle (EV) charging to increase local use and resilience. The Hybrid Artificial Neural Network-Integrated Synergistic State-of-Charge Supervised Power Management System (HANNI-S^3-PMS) operated in both grid-connected and islanded modes on an AC/DC MG. Control was hierarchical: primary proportional–integral loops regulated converter currents and voltages; an artificial neural network (ANN) provided maximum-power-point tracking (MPPT) for PV and wind and decentralized power sharing; and a tertiary state-of-charge (SoC)-supervised layer coordinated power flows and charging via ANN optimization with phase-locked-loop (PLL) synchronization for seamless transitions. MATLAB/Simulink studies spanning varied loads, renewable ramps, and grid contingencies showed near-complete renewable capture, exceptionally fast transient recovery, tightly regulated DC-bus voltage with minimal overshoot and quick settling, and resilient load balancing, while reducing reliance on the utility grid and curbing storage stress. Frequency-domain and time-domain analyses verified stability, and comparisons with representative MG controllers indicated higher efficiency with low computational overhead. HANNI-S^3-PMS provided a data-driven alternative to computationally heavy optimizers, significantly removed dependence on pre-tuned parameters, scaled to real-time multi-node deployment, and advanced autonomy, reliability, and seamless grid/island operation in HMG.

1. Introduction

The global transition of renewable energy is also increasing rapidly with countries aiming to achieve ambitious sustainability goals, which drives substantial progress in grid-connected MG scheduling controllers to optimize distributed generation and enhance reliability [1], and the creation of smart energy management systems that can reduce grid reliance, decrease operational expenses, and optimize economic performance through dynamically integrated tariffs [2]. According to modelled energy transition pathways, achieving the Paris Agreement targets requires global net CO_2 emissions to fall by roughly 45 % by 2030, with much of this reduction driven by accelerated renewable deployment. The declining cost of solar, wind, and battery storage has already made HMG solutions increasingly competitive compared to conventional fossil-based generation [3]. Although they are important in the decarbonization process, the renewable sources of power like solar and wind have inherent variability and forecasting uncertainty, which present system stability challenges, operational reliability, and long-term system planning [4]. MGs are considered as a solution to these problems, as they allow localized integration of renewable energy sources (RESs) and facilitate flexible operation in both grid-connected and islanded modes, thus enhancing the overall network resilience [5]. In this framework, grid-connected HMG systems play a crucial role as interfaces between distributed renewable generation, and the main

* Corresponding author.
E-mail address: mazaher.karimi@uwasa.fi (M. Karimi).

https://doi.org/10.1016/j.ecmx.2025.101316
Received 12 August 2025; Received in revised form 16 September 2025; Accepted 1 October 2025
Available online 2 October 2025

utility grid, enabling coordinated power exchange, optimal dispatch and enhancement of techno-economic and environmental performance [6]. The integration of PV and wind power in HMGs is especially beneficial, as the complementary nature of the production pattern between the two sources- PV throughout the day, and wind generation during the night and seasons- results in a more stable supply profile, increased stability in the network, and a lack of reliance on a single energy source [7,8]. However, due to the intermittency of these resources, energy imbalances are a common occurrence thus the need to deploy energy storage systems and advanced energy management mechanisms to maintain secure, reliable and economical operation [9].

Single ESS, like batteries, have short lifespan and degrade quickly in frequent cycling in MGs, whereas SCs alone cannot store sufficient energy and are therefore individually inadequate; hence hybrid ESSs are favored to respond to dynamic loads and renewable fluctuation with confidence [10,11]. Combining batteries and SCs in the form of HESS allows matching power and energy density, which results in extended storage, increased reliability, and reduced costs in MGs [9,12]. The grid-connected MGs are associated with complex coordination between volatile RESs, HESSs, dynamic loads, and market-based interaction with the grid, which demands multi-layered predictive control in order to guarantee stability, resiliency, and optimality in energy trading [13,14]. The problem of real-time optimization of power dispatch in grid-connected MGs is extremely challenging due to the unpredictable nature of renewable energy, variability in loads, and operational constraints of HESS that requires advanced and intelligent energy management systems that guarantee effective MGs operations [15,16]. While significant progress has been made in the control of individual RESs and ESSs, integrated modeling, coordinated control, and real-time optimization of hybrid RES-HESS configurations in grid-connected MGs remain underexplored, limiting their operational efficiency and resilience [17]. Recent studies report that grid codes in Europe and Asia-Pacific enforce frequency stability limits of ±1 % and voltage variations within ±2 %, requiring MGs to dynamically restore nominal values within seconds after a disturbance, which has driven the adoption of hierarchical and advanced control strategies for distributed storage and generation [18]. This paper presents a detailed framework for modeling, controlling, and assessing the performance of an HMG system with grid integration, ANN-based MPPT for both PV and wind, and SoC based ANN-controlled HESS supplying AC and EV loads. The system is built on the Autonomous HANNI-S^3 Controlled hybrid energy architecture to ensure coordinated RES-HESS-grid operation, with ANN-based controllers employed as lightweight, data-driven alternatives to heavy optimization, enabling real-time control and scalability under dynamic conditions [19].

1.1. *Existing works on grid-connected MGs with hybrid energy sources and storage systems*

Existing literature on grid-connected MGs with hybrid energy sources and storage systems demonstrates various methodologies, which are aimed at optimizing energy management and maintaining system stability. Several studies have explored sophisticated control strategies to improve renewable utilization, DC-bus stability, and load management efficiency.

Argyrou et al. (2021) proposed a power management technique that uses filtration-based method which combines PV and HESS to reduce the grid's influence, to ensure DC-bus voltage is more stable, and reduce battery degradation during transient conditions. Their approach lacks comprehensive stability assessments across diverse load profiles and mixed-mode scenarios with simultaneous DC and AC load variations [20]. Similarly, Kumar and Bae (2022) developed a dynamic power management system employing Model Predictive Control (MPC) to optimize inverter performance and mode transitions. While moving average filter (MAF) has many advantages, it causes delays in high-frequency events and does not consider situations where backup from the grid is required during energy deficits [21].

Other approaches, mainly droop control, are being explored in adaptive control strategies. Kandari et al. (2023) introduced a hybrid controller that uses State of Charge (SoC)-based adaptive droop control and FLC-PI controllers to ensure better stability when the load is switched in hybrid AC/DC MGs. However, their approach does not change over time to account for changing loads or uncertain generation from RES. Thus, limiting its optimization capabilities [22]. Likewise, Abouobaida et al. (2023) introduced an energy management system (EMS) that applies fuzzy logic controllers (FLC) and sliding mode control (SMC) to a standalone DC MG. But the studies do not consider a range of AC/DC mixed load scenarios and do not fully examine the behaviors of batteries and SCs during extreme or absent conditions [23].

Bhattar and Chaudhari (2023) suggested optimization-based energy management approaches using linear programming (LP) and mixed-integer linear programming (MILP) to boost the use of renewable energy, maintain stable DC bus voltage, and handle loads in centralized MGs. On the other hand, scalability of their model beyond small-scale applications remains untested, and computational efficiency concerns for larger distributed systems persist [24]. Additionally, Farrokhi et al. (2024) introduced an optimization-based PMS that uses Adaptive Kalman Filtering (AKF) and Karush-Kuhn-Tucker (KKT). Nevertheless, being sensitive to minor changes in parameters and not being able to directly control SCs makes the system less responsive when load changes [25].

In their studies (2023), Patel et al. presented two new methods which utilizes hybrid fuzzy-integrated fractional-order PID (FOPID) and hybrid adaptive fuzzy-integrated fractional-order PD-PI (HAFI FPD-PI) controllers to improve the stability of the DC bus voltage and the synchronization of the inverter. Despite these proposed advancements, validation under extreme or highly variable conditions is limited, and controller complexity poses real-world implementation challenges [26,27]. In a similar manner, Soliman et al. (2021) introduced supervisory EMS with fuzzy high-order sliding mode control (FSHSMC), yet accurate predictions of renewable energy are still necessary, as inaccuracies might result in the inefficiency of the system [28].

Different approaches have been contributed by other studies. Bai et al. (2020) linked real-time demand-side management with hybrid dynamic modeling, even, depending solely on set profiles hindered the evaluation of adaptability in uncertain situations [29]. Sandeep and Mohanty (2023) proposed Artificial Rabbits Optimized Neural Networks (ARONN) for isolated MG, highlighting concerns about fixed weight parameters and unexplored fault tolerance [30]. In the study by Kamel et al. (2019), PI control was used for both batteries and fuel cells, whereas direct SC connections can result in uncontrolled charge or discharge and poor performance in response to sudden changes [31]. Manandhar et al. (2019) designed a dynamic EMS based on battery SoC for HESS, though severe transient and multi-source variability effects remain inadequately addressed in the proposed system [32]. Although Shuvo et al. (2025) examined how load can be managed in grid-isolated DC MG, considerations about other sources of renewable energy and scaling should be explored further [33].

In conclusion, these studies have made great advancements in developing different control and optimization methods. However, as summarized in Table 1, gaps persist, particularly regarding scalability, adaptability under extreme conditions, and integration of diverse renewable sources and dynamic load scenarios. Therefore, providing chances for additional research and advancement.

1.2. *Identified gaps in existing works*

Based on the findings from the literature review, it is evident that although HMG systems have been widely explored, several important areas remain insufficiently addressed. These shortcomings reduce system flexibility, hinder real-time performance, and limit their suitability for complex, real-world applications. The key gaps identified across the

Table 1
Literature Review Summary of Control Strategies, Stability Analysis, Contributions, and Limitations for Hybrid Energy Systems in MG Applications:

Ref	System	Topology	Control strategy	Bus voltage regulation	Controller modeling	Stability analysis	Key points
20	PV/battery/SC	Grid connected MG with AC load	Filtration-Based PMA with PI Controllers	± 0.625 %	✓	✓	− Battery-SC hybridization reduces battery stress and increases lifespan.− Achieves DC-bus voltage stability with minimal ripple (±0.625 %).
21	PV/battery/SC/fuel cell	Grid connected MG with DC load	Model Predictive Control (MPC)-based Dynamic PMS	± 4 %	✓	✓	− Decoupled active/reactive power control using MPC.− MAF causes phase lag and ignores grid backup, limiting dynamic adaptability.
22	PV/battery/SC/fuel cell	Standalone hybrid AC/DC MG	SoC-based Adaptive Droop Control with FLC-PI	–	–	–	− Event-wise power flow adaptation− FLC-PI reduces SC power deviation by up to 90 % during transients.−SoC-based droop control lacks adaptability to load and generation variations, limiting optimization.
23	PV/Wind/Battery/SC	Standalone DC MG with DC & AC loads	Fuzzy Logic Control (FLC) for MPPT, Sliding Mode Control (SMC) for EMS	±0.25 %	✓	–	− MPPT via FLC outperforms P&O and INC-COND.− SMC ensures fast DC bus regulation (400 V, ±1 V).−Validation lacks diverse AC/DC and intermittent load scenarios.
24	PV/BESS	Grid-connected DC load MG	Centralized Energy Management Scheme (CEMS) with hierarchical multi-optimization (LP & MILP)	±5.83 %	✓	–	− LP and MILP used for optimal PV-BESS use and prioritized load shedding.− Maintains 48 V DC bus with high reliability and real-time performance.−Scalability beyond 1.2 kW and computational efficiency for large MGs remain unverified.
25	Battery/SC	Standalone DC MG with AC load	Adaptive Kalman Filter (AKF) and KKT-based multi-objective optimization	<±5%	✓	–	− Accurately estimates grid current with less than 1.5 % error.− Experimental results show a 50 % improvement in battery lifespan.−Semi-active HESS lacks SC control, limiting response to rapid load shifts.
26	PV/Wind/Battery/SC	Isolated hybrid MG with DC & AC loads	Hybrid Adaptive Fuzzy Integrated Multistage FOPID + nVdPO-based VOC	±2%	✓	✓	− Maintains stable 50 V DC grid.− VOC ensures synchronized inverter output.−Limited PMS validation and non-adaptive HHO tuning reduce flexibility under dynamic conditions.
27	PV/Wind/Battery/SC	Standalone DC load MG with DC load	Hybrid Adaptive Fuzzy Integrated Fractional Order PD-PI (HAFI FPD-PI)	±4.2 %	✓	✓	− Enhances voltage stability with ± 2.1 V deviation (≤5%).− Power-sharing between SC and battery reduces battery stress.
28	PV/Wind/Tidal/Battery	Smart grid-integrated DC MG with EV & smart university loads	Fuzzy Supervisory High-Order Sliding Mode Control (FSHSMC)	<±10 %	✓	–	− Combines MPPT and off-MPPT modes based on SoC and load.−Renewable variability makes accurate forecasting crucial; errors cause energy surplus or shortage.
29	PV/Battery/SC/DG/Public Grid	Grid-connected & islanded DC load MG	Rule-based real-time energy management algorithm with load shedding optimization	<±10 %	–	–	− Real-time load optimization via MILP.− Priority-based source usage.−Uses fixed profiles, limiting adaptability under dynamic high-demand, low-generation scenarios.
30	PV/Battery/SC	Isolated DC load MG	Artificial Rabbits Optimized Neural Network (ARONN) EMS	<±10 %	✓	–	− Combines ANN and ARO to optimize battery/SC current control.− Reduces battery stress, enhances SoC control.−Fixed NN weights and untested fault tolerance reduce adaptability and reliability.
31	PV/Fuel Cell/Battery/SC	Standalone DC MG with 3-phase AC load	Classic PI-based EMS	–	–	–	− Direct SC-DC connection reduces cost and response time.−Fuel cells respond slowly to load changes, affecting power stability.
32	PV/Battery/SC	Grid-connected DC MG with DC & AC loads	Sharing Coefficient-based Power Allocation	±2.9 %	✓	–	− Reduces battery stress by dynamically adjusting power sharing based on SoC.− Efficient control of charge/discharge rates to extend battery life.−PMS lacks consideration for severe load transients and multiple variable renewables.
33	PV/Battery/SC	Grid-isolated DC MG with DC & AC loads	Fuzzy Logic-based MPPT with Adaptive Load Management	±2.5 %	✓	✓	− Optimizes power output and stability across various load scenarios.

reviewed studies are summarized below:

- Many studies adopt simplified assumptions, using static load/generation profiles and single-source renewable inputs (mainly solar). This overlooks dynamic scenarios (AC/DC variations, severe imbalances) and hybrid setups with wind or grid backup, reducing practicality and robustness.
- Control and optimization strategies in MGs often lack adaptability and scalability for real-time operation. Many approaches provide only limited coordination of energy storage, rely on pre-tuned or non-adaptive control settings, or involve optimization techniques with high computational demands.
- Reviewed MG frameworks show limited adaptability and robustness under real-world fluctuations; evaluations are mostly restricted to narrow operating conditions, leaving efficiency, resilience, and reliability under realistic or extreme scenarios insufficiently validated.
- SOC limits of batteries and SCs are frequently neglected, while stability analyses (both frequency- and time-domain) compared with existing approaches are limited. These gaps risk deep charge–discharge cycles, reduced battery lifetime, and unvalidated long-term reliability under stressed conditions.

1.3. Contribution of the proposed work in addressing existing limitations

Despite significant progress in HMG research, critical limitations persist in system adaptability, real-time performance, energy source integration, and control stability. The proposed work directly addresses these gaps by introducing a comprehensive, intelligent control framework designed for robust, real-world operation. Leveraging advanced ANN-based strategies, multi-source energy integration, and dynamic storage coordination, the system enhances energy efficiency, stability, and scalability. The following objectives outline the key contributions of this study in overcoming the shortcomings identified in existing literature.

- Proposed HANNI-S^3-PMS, a grid-interactive framework integrating PV, wind, grid support, battery–SC storage, and EV charging on an AC/DC MG, enabling adaptive load management, real-time demand response, reduced grid dependence, and improved resilience under dynamic conditions.
- Introduced an ANN-based hierarchical control combining PI loops for current–voltage regulation, and a tertiary SoC-supervised layer for storage and EV coordination. Achieved renewable capture ≈ 1, transient recovery $\leq$10 ms, and DC-bus overshoot $\leq \pm 0.88$ V ($\approx$ 1.76 %) while significantly eliminating pre-tuned parameters and heavy optimizers, ensuring real-time multi-node deployment.
- Developed SoC–aware coordination enforces battery/SC limits, schedules charge/discharge (incl. EV), and assigns fast transients to the SC to reduce deep cycling and lower battery stress, improving longevity.
- Demonstrated rigorous stability and performance validation through frequency-domain (Bode plot) and time-domain (step response) analyses, and validated the framework through 15 dynamic case studies under varied loads, fluctuations, and extreme scenarios confirmed tighter voltage regulation, balanced sharing, reduced grid imports, and low computational burden.

This paper is structured as follows: Section 2 outlines the modeling and control strategy of the proposed grid-connected MG system. Section 3 demonstrates comprehensive stability and transient response analysis with existing proposed controllers. Section 4 explains the power management strategy algorithm for the proposed hybrid grid-connected MG system. Section 5 presents the simulation results of 15 cases grouped into 4 scenarios carried out in MATLAB/Simulink. Section 6 provides a comparative analysis with existing studies. Lastly, Section 7 concludes the paper.

2. Modeling and control strategy of the proposed grid-connected MG system

2.1. Proposed ANN-Based hybrid energy storage and source system Grid-Connected MG

The architecture of a dual-mode grid-interactive energy management

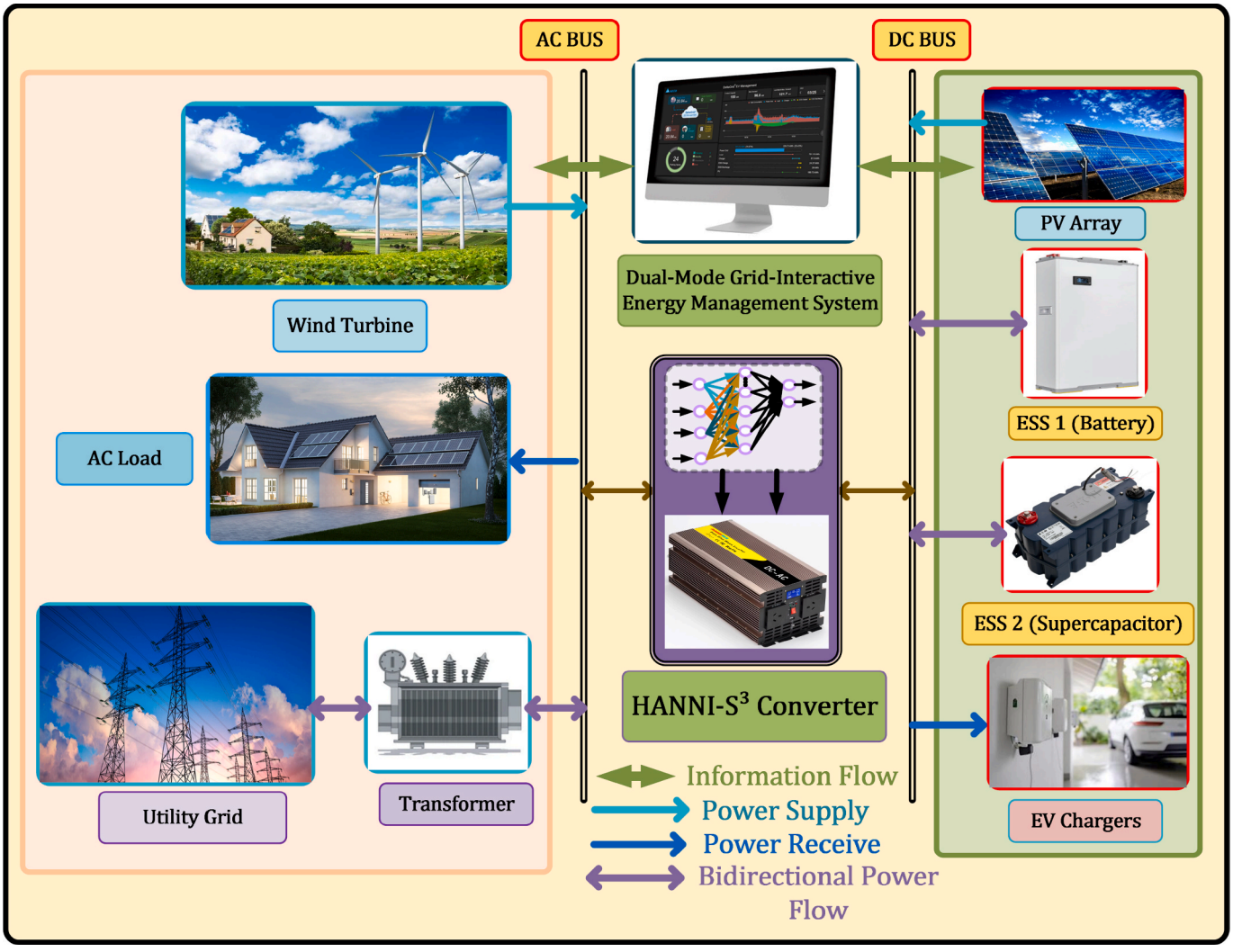

Fig. 1. Block diagram of the proposed ANN-based hybrid energy storage and source system grid-connected MG.

system that combines both DC and AC MG components is shown in Fig. 1. Wind turbines, the utility grid (via a transformer) supply power on the AC side, which is distributed to residential AC loads. PV arrays produce electricity on the DC side, and are connected to two forms of ESS, an ESS based on a battery (ESS 1) and another ESS based on SC (ESS 2). The DC bus is also connected to EV chargers. The core of the system is the HANNI-S^3 converter, which allows the power to be exchanged between the DC and AC buses in both directions and allows the renewable sources and storage units to be easily integrated into the system. A dual-mode energy management system supervises the entire setup, coordinating power supply, demand response, and bidirectional energy flows to optimize system reliability, efficiency, and stability. The diagram depicts distinct flows: information exchange, unidirectional power supply and reception, as well as bidirectional power transfer, highlighting the coordinated interaction between generation, storage, and load components.

This proposed control allows seamless integration of RESs and storage, optimizing system performance. The system is designed to meet both local and grid demands, ensuring reliability, stability, and sustainability. The combination of ANN optimization and hybrid components enhances the system's efficiency and adaptability, supporting a clean and reliable energy infrastructure.

Table 2 lists the specifications and operating parameters considered for the proposed grid-connected HMG system, covering power sources, energy storage, loads, and converter components.

2.2. PV system with ANN-based MPPT control

The PV array is connected with a DC-DC boost converter and an ANN-based MPPT controller in the system. The ANN MPPT system sets the optimum duty cycle by using the PV voltage, temperature, and irradiance, and implements it using a PID-controlled PWM generator for better power extraction [34,35]. The PV output current is [34]:

Table 2
Specifications of parameters of the proposed grid-connected HMG System.

S. no	Description	Values	Unit
	PV voltage	20.2	V
1	PV current	7.43	A
	PV power	7650	W
	Wind voltage	48	V
2	Wind current	125	A
	Wind power	6000	W
	Battery voltage	47	V
3	Battery rating	400	Ah
	SoC	15–100	%
	Nominal discharge current	173.91	A
	SC voltage	48	V
4	SC capacitance	28,125	F
	SoC	15–100	%
	AC Constant load	2000	W
5	AC Varying load	0 4000	W
	EV Constant Load	1300	W
6	EV Varying Load	0 2600	W
	Battery converter inductor	1.06e-4	H
7	Battery converter capacitor	0.0060	F
	SC converter inductor	0.0011	H
8	SC converter capacitor	0.0130	F
	Switching frequency	10	kHz
9	Battery current controller gain	K_p^{Bat} = 8.2e-7, K_i^{Bat}= 0.164	–
	SC current controller gain	K_p^{SC} = 8.17e-7, K_i^{SC}=0.163	–
	PV Boost converter inductor	4.304e-4	H
10	PV Boost converter capacitor	0.165	F
	Switching frequency	10	kHz
11	Wind Buck converter inductor	0.320	H
	Wind Buck converter capacitance	6.25e-5	F
12	Grid frequency	50	Hz
	Grid Voltage	220	V
13	DC bus voltage controller gain	K_P = 0.1493, K_i= 0.1783	–
	DC bus voltage	50	V

$$I_{PV} = I_L - I_d\left(exp\left(\frac{V_{PV}+I_{PV}R_S}{aV_T}\right)\right)-1)-\frac{V_{PV}+R_SI_{PV}}{R_P} \quad (1)$$

In Eq. (1), I_L is a light-generated current, I_D is diode current, V_{PV} and I_{PV} is PV module voltage and current, the losses across the series resistance R_S and the shunt resistance R_P, V_T is thermal voltage.

2.2.1. Ann-based MPPT control for PV system

Fig. 2 shows the ANN implemented for MPPT predicts the optimal operating voltage V_{MPPT} of the PV system under varying environmental conditions. The architecture comprises an input layer that accepts temperature (T) and irradiance (G), a hidden layer with activation functions, and an output layer that computes V_{MPPT}. Each hidden neuron processes T and G through its respective weights and biases, with the output of the j-th hidden neuron given as [36]:

$$z_j = f\left(w_{Tj}.T + w_{Gj}.G + b_j\right) \quad (2)$$

The final output, V_{MPPT}, is calculated in the output layer by aggregating the contributions from all hidden neurons as:

$$V_{MPPT} = f_{out}\left(\sum_{j=1}^{m} w_j f\left(w_{Tj}.T + w_{Gj}.G + b_j\right) + b_{out}\right) \quad (3)$$

In Eqs. (2)–(3), w_{Tj} and w_{Gj} are the weights for inputs T and G for the j-th neuron, b_j s its bias, and f and f_{out} are the activation functions for the hidden and output layers.

2.2.2. Training and performance evaluation of ANN-based MPPT for PV system

The training process utilizes simulated datasets of T, G, and their corresponding V_{MPPT}. The network minimizes the mean squared error (MSE) between the predicted $(\widehat{V}_{MPPT})$ and actual (V_{MPPT}), calculated as [36]:

$$MSE = \frac{1}{N}\sum_{i=1}^{N}\left(V_{MPPT,i} - \widehat{V}_{MPPT,i}\right)^2 \quad (4)$$

In Eq. (4), $V_{MPPT,i}$ is the actual voltage, $\widehat{V}_{MPPT,i}$ is the predicted voltage, N is the number of training samples. The network iteratively updates weights and biases through backpropagation as follows:

$$w_{t+1} = w_t - \eta\frac{\delta MSE}{\delta b}, b_{t+1} = b_t - \eta\frac{\delta MSE}{\delta b} \quad (5)$$

In Eq. (5), w_t and b_t are the current parameters, η is the learning rate, and the derivatives represent how MSE changes with respect to weights and biases.

The quick drop in MSE in the early epochs, as seen in Fig. 3, indicates that the system is learning effectively and improving continuously

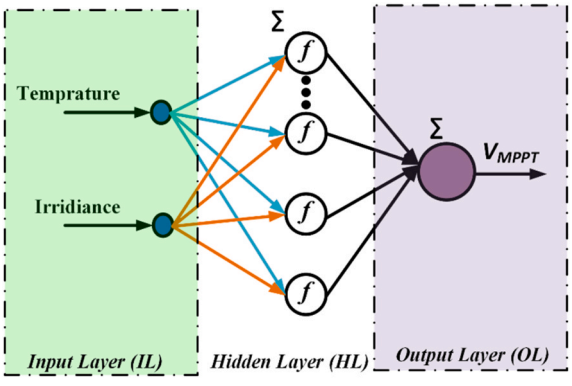

Fig. 2. ANN architecture for PV system MPPT control [36].

toward low error afterward. Due to this advanced strategy, the ANN can respond well to changes in the environment and obtain the best validation MSE of 4.0532×10^{-11} at epoch 1000.

According to Fig. 4, the ANN-based MPPT controller has a high regression coefficient (R = 1) across training, validation, testing, and overall data. This indicates a perfect linear relationship between the predicted $\widehat{V}_{MPPT}$ and actual V_{MPPT}, with the regression equation approximated as [34]:

$$\widehat{V}_{MPPT} \approx V_{MPPT} + \epsilon_i \tag{6}$$

In equation (6), V_{MPPT} is the actual voltage, $\widehat{V}_{MPPT}$ is the predicted voltage, ϵ_i represents a negligible error offset close to zero.

2.3. Wind energy conversion system modelling with ANN-based MPPT control

In our wind energy system, the Permanent Magnet Synchronous Generator (PMSG) powered by the turbine produces power that is converted to DC and stabilized by a buck converter to maintain the DC bus output voltage stable [37,38]. The duty cycle is adjusted in the ANN-based MPPT controller using turbine voltage and current, and the PID controller manages the power through the converter. The turbine power output is governed by [38]:

$$P_{turbine} = \frac{1}{2}\rho A C_p(\lambda, \beta) v_w^3 \tag{7}$$

In Eq. (7), v_w is the wind speed, ρ is air density, A is rotor area, and C_p is the power coefficient, which represents the efficiency of energy conversion.

2.3.1. Ann-based MPPT control for wind turbine system

The ANN-based MPPT method has also been adapted for wind turbines to handle the rapid fluctuations in wind speed and rotor dynamics. Wind turbines, unlike PV systems, depend on the instantaneous changes in voltage and current. In Fig. 5, the ANN is used to determine the optimal operating voltage, with each hidden neuron handling voltage and current by using its weights and biases [38]:

$$z_j = f\left(w_{Vj}.V + w_{Ij}.I + b_j\right) \tag{8}$$

$$V_{MPPT} = f_{out}\left(\sum_{j=1}^{m} w_j f\left(w_{Vj}.V + w_{Ij}.I + b_j\right) + b_{out}\right) \tag{9}$$

In Eqs. (8)–(9), w_{Vj} and w_{Ij} are voltage and current weights, b_j is the hidden neuron bias, and f s its activation function. The hidden neuron outputs are combined using output weights w_j, b_{out}, and activation f_{out} to produce the final output V_{MPPT}.

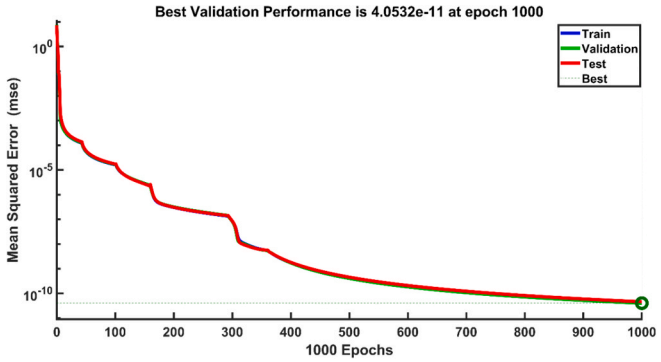

Fig. 3. Training performance of the ANN-based MPPT control for PV system.

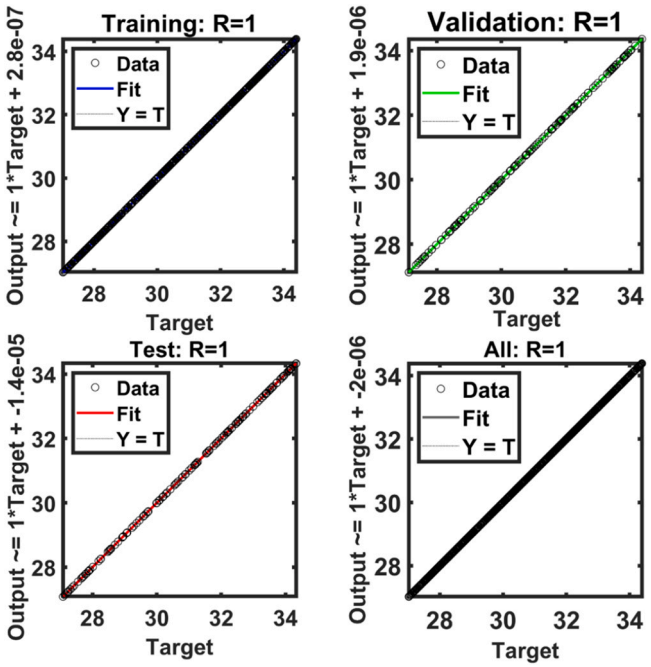

Fig. 4. Neural network performance for PV system: training, validation, test, and overall.

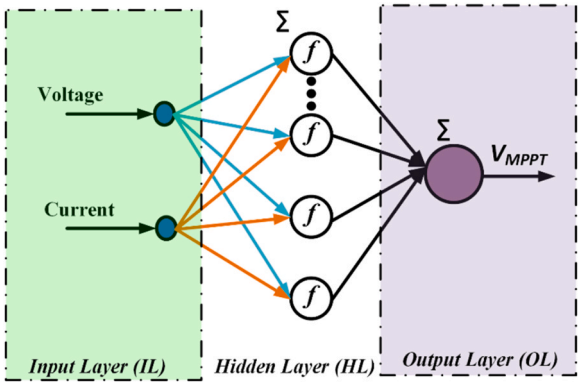

Fig. 5. ANN architecture for wind turbine MPPT control [38].

2.3.2. Training and performance evaluation of ANN-based MPPT for wind turbine system

The wind turbine's ANN-based MPPT uses the same equations (Eq. (4)–(5)) as the PV system, adding wind-related features to handle fast fluctuations in voltage and current. The ANN achieved the best validation performance of 1.5205×10^{-6} MSE at epoch 332, as shown in Fig. 6. At epoch 50, the validation error dropped significantly from 10^0 to 10^{-5}, with further reduction to 10^{-6} by epoch 332. Lastly, normalizing the data and using adaptive learning rates helped the model stay stable and give accurate predictions for different wind speeds.

The ANN-based controller for the wind turbine system efficiently performs as it achieves a regression coefficient (R = 1) on all training, validation, testing, and overall datasets, as illustrated in Fig. 7. The predicted operating voltage $\widehat{V}_{MPPT}$ aligns closely with the actual voltage V_{MPPT}, with minimal error offset, as represented by the regression relationship derived in Eq. (6) in the previous section.

2.4. Ann-based control for the hybrid energy storage system

The HESS ANN-based controller is based on the same structure used

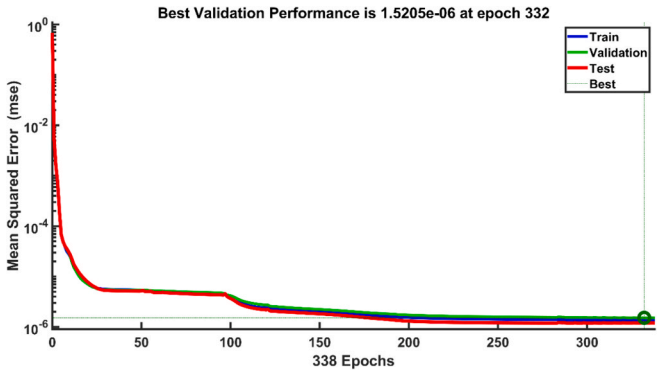

Fig. 6. Training performance of the ANN-based MPPT control for Wind turbine system.

in PV and wind systems, but it is designed to handle the different behaviors of the battery and SC. Fig. 8 displays the Input Layer (IL), Hidden Layer (HL), and Output Layer (OL). The IL processes key inputs: I_{Bat_ref}, I_{Bat_error}, I_{SC_error}, and I_{SC_ref}, essential for regulating charge–discharge cycles. The HL improves these signals and passes them to the OL, which sends the control signals δ_{Bat} and δ_{SC} to optimize energy flow and system efficiency [39].

The input vector is defined as:

$$X = \begin{bmatrix} I_{Bat\_ref} \\ I_{Bat\_error} \\ I_{SC\_ref} \\ I_{SC\_error} \end{bmatrix} \tag{10}$$

In Eq. (10), I_{Bat_ref} and I_{SC_ref} are the reference currents, while I_{Bat_error} and I_{SC_error} are the current errors of the battery and SC.

The HL processes these inputs by applying activation functions, with the output from each hidden neuron being calculated as follows [39,40]:

$$h_j = f_1\left(\omega_{j1}.I_{Bat\_error} + \omega_{j2}.I_{Bat\_ref} + \omega_{j3}.I_{SC\_error} + \omega_{j4}.I_{SC\_ref}\right) + b_j \tag{11}$$

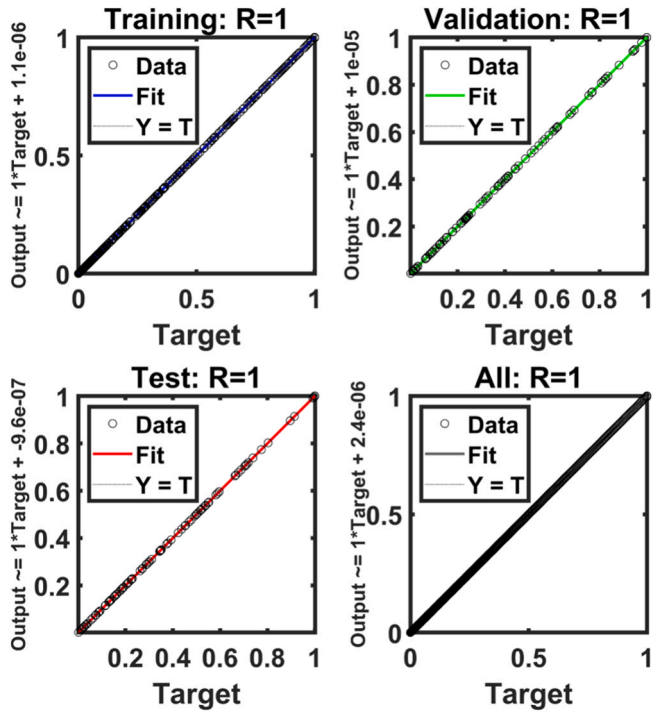

Fig. 7. Neural network performance for wind turbine: training, validation, test, and overall.

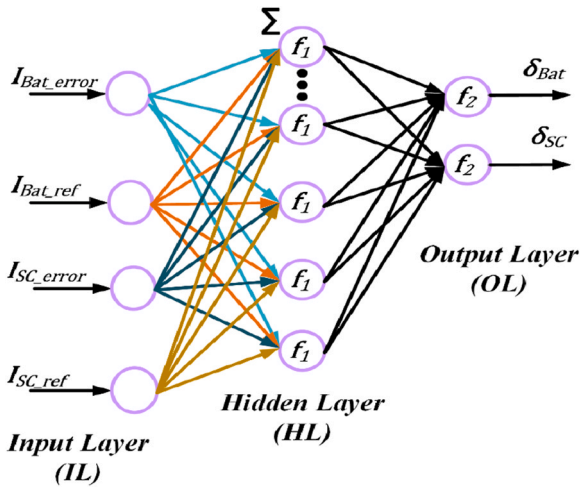

Fig. 8. Supervised feed-forward artificial neural network structure for HESS [39].

In Eq. (11), $\omega_{j1}, \omega_{j2}, \omega_{j3}, \omega_{j4}$ are the weights associated with the respective inputs, b_j is the bias for the hidden neuron, and f_1 is the activation function applied at the hidden layer. The output layer aggregates the contributions from all hidden neurons to compute the final adjustments for the battery and SC as follows [39,40]:

$$\delta_{Bat} = f_2\left(\sum_{j=1}^{n} \omega_j^1.h_j + b_{Bat}\right) \tag{12}$$

$$\delta_{SC} = f_2\left(\sum_{j=1}^{n} \omega_j^2.h_j + b_{SC}\right) \tag{13}$$

In Eqs. (12)–(13), ω_j^1 and ω_j^2 are the weights connecting the hidden layer to the output layer for battery and SC adjustments, b_{Bat} and b_{SC} are the biases, and f_2 is the activation function at the output layer.

2.4.1. Training and performance evaluation of ANN-based control for HESS

The training process of the ANN-based control strategy for the HESS is assessed by monitoring the MSE is:

$$MSE = \frac{1}{N}\sum_{i=1}^{N}(y_i - \hat{y}_i)^2 \tag{14}$$

In Eq. (14), y_i are the actual target values, $\hat{y}_i$ are the predicted outputs, and N is the number of samples.

In Fig. 9, the MSE reduces a lot during the beginning epochs, which indicates smooth learning. The results for the training, validation, and test datasets are very similar, and validation reaches its highest value of 2.1489×10^{-6} at epoch 1000. The training and test curves, shown in blue and red, converge towards the optimal performance, confirming the ANN's effectiveness in minimizing prediction errors.

The overall performance of the ANN-based control system on HESS is examined by regression analysis, as indicated in Fig. 10, where the (R = 1) for all the datasets. This indicates a perfect linear relationship between the predicted and actual outputs.

2.5. Proposed hybrid artificial neural network–integrated synergistic SoC-supervised (HANNI-S^3) controller

In Fig. 11 the HANNI-S^3 controller introduces a unified, intelligent energy management framework that tightly couples ANN-based MPPT, droop control, and SoC-supervised supervisory control for HMG

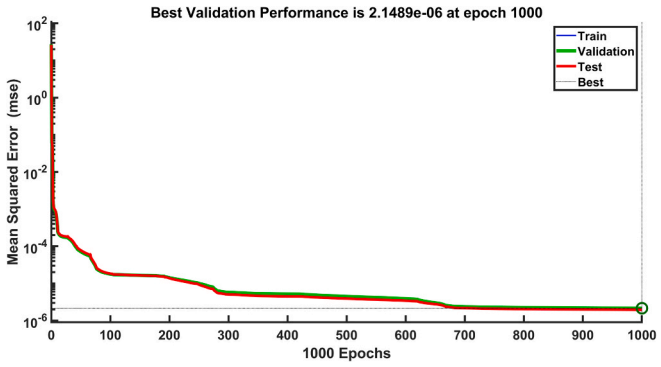

Fig. 9. Training performance of the ANN-based HESS.

applications. At the primary control level, high-bandwidth PI controllers with PWM modulation regulate converter currents and voltages, ensuring rapid dynamic response. A feed forwarding ANN-based scheme at the secondary level provides a decentralized power sharing and frequency/voltage support, which in turn mitigates the need to rely on constant communication. The tertiary supervisory layer combines real-time SoC monitoring and predictive ANN-based power optimization to coordinate PV, wind, battery, SC, and grid power flows, thus making suitable buck/boost choices and balancing charging/discharging operations. This multi-layered architecture allows easy transitions in the event of source intermittency, optimum local power utilization, and a smooth grid synchronization by PLL-based control. By embedding decision-making both locally and at the supervisory level, the HANNI-S^3 controller ensures deterministic, delay-tolerant operation and enhances MG resilience, representing a significant advancement over conventional centralized or purely droop-based schemes.

3. Comprehensive stability and transient response analysis with State-of-the-Art controllers

To highlight the novelty and practical significance of the proposed controller, this section presents a comprehensive comparative evaluation with several representative state-of-the-art controllers [21,26,27,33]. The analysis combines frequency-domain (Bode) and time-domain (step) analyses and allows a comprehensive exploration of major performance measures such as bandwidth, phase margin, damping ratio, overshoot, settling time, and the overall quality of transient response. This dual-domain study provides an in-depth overview of the dynamic behavior of the controller and underlines its ability to offer improved stability margins and faster, well-damped transient behavior than conventional systems. Equation (15) present the stability analysis of the HANNI-S^3 Controller is based on its transfer function [41]:

$$G_{System}(s) = \frac{10947.29s + 1431.74}{0.165s^2 + 0.01s + 5.77} \tag{15}$$

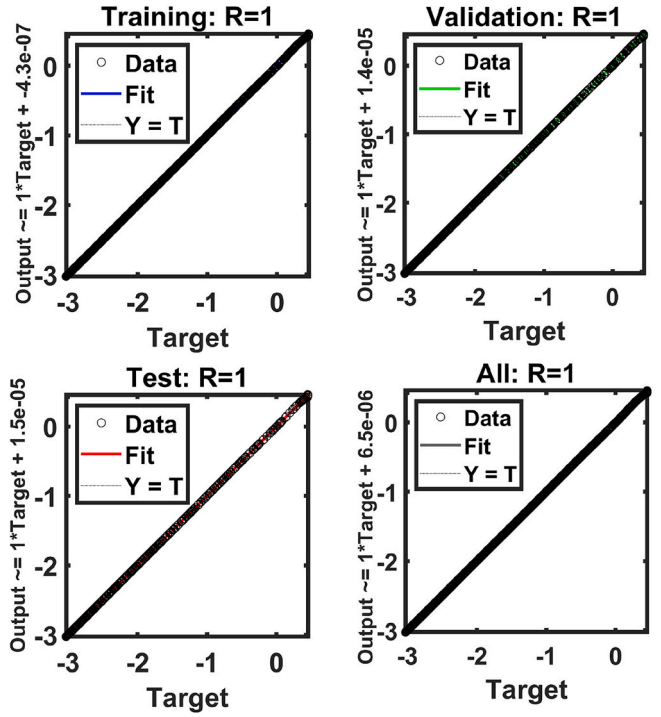

Fig. 10. Neural network performance for HESS: training, validation, test, and overall.

3.1. Frequency-domain evaluation

Fig. 12 shows the Bode plots for the proposed HANNI-S^3 controller and four representative designs from the literature. The proposed controller maintains $\approx 0^{\circ}$ phase up to $\approx 10^2 rad/s$, then rolls off smoothly to $\approx -60^{\circ}$ near $10^3 rad/s$ and $\approx -135^{\circ}$ at $10^4 rad/s$. This gradual decrease supports a phase margin above 60° at its unity-gain crossover near $5 \times 10^2 rad/s$, ensuring robust stability and well-damped transient response.

In contrast, [26] shows earlier phase lag, reaching $\approx -60^{\circ}$ already near $10^2 rad/s$ and approaching $\approx -180^{\circ}$ by $10^5 rad/s$. This results in a much lower phase margin at its crossover frequency $(\approx 1.5 \times 10^2 rad/s)$, making it more conservative but slower to respond.

Both [21] and [27] display rapid phase roll-off near $10^2 rad/s$,with $\approx -45^{\circ}$ lag coinciding with their gain peaking. They cross -90° earlier $(\approx 2 \times 10^2 - 5 \times 10^2 rad/s)$, leading to reduced phase margins and potentially oscillatory closed-loop behavior. Their phase approaches $\approx -150^{\circ}$ by $10^4 rad/s$, leaving little margin against instability at higher frequencies.

Finally, [33] exhibits a phase profile close to the proposed design, remaining near 0° up to $10^2 rad/s$ and reaching $\approx -60^{\circ}$ near $10^3 rad/s$. Its crossover frequency is lower $(2 \approx \times 10^2 rad/s)$, resulting in a moderate phase margin, which is slightly below the proposed controller but still indicating good stability and well-controlled dynamics.

3.2. Time-domain evaluation

The step responses demonstrated in Fig. 13 highlight the superior dynamic performance of the proposed control scheme. The proposed controller exhibits an exceptionally fast and well-damped transient response, characterized by an ultra-short rise time ($t_r \approx 0.01ms$) and a very short settling time ($t_s \approx 0.015ms$). The absence of overshoot ($M_p = 0\%$) and oscillations confirms that the system operates in a critically or slightly over-damped regime ($\zeta \geq 1$). This combination ensures minimal transient stress on power components and excellent voltage regulation even under abrupt load disturbances.

In contrast, Reference [33] achieves a clean but slower response, with ($t_r \approx 1ms$) and ($t_s \approx 1.8ms$), while still maintaining zero overshoot. This indicates stable, non-oscillatory behavior, though its slower transient performance renders it less suitable for applications requiring ultra-fast regulation.

Reference [21] provides a relatively faster rise time ($t_r \approx 0.9ms$), but exhibits light underdamping, as evidenced by a moderate overshoot of ($M_p = 5\ 8\%$) and a longer settling time ($t_s \approx 4.5ms$). This reflects a damping ratio in the range of ($\zeta \approx 0.6 - 0.7$), resulting in mild overshoot but still offering a good compromise between speed and stability.

Finally, References [26] and [27] demonstrate the slowest and least well-damped behavior, with ($t_r \approx 4ms$), ($t_s \approx 16 - 18ms$), and significant overshoot ($M_p = 15\ 18\%$). The pronounced oscillatory nature of the response, associated with a damping ratio of approximately

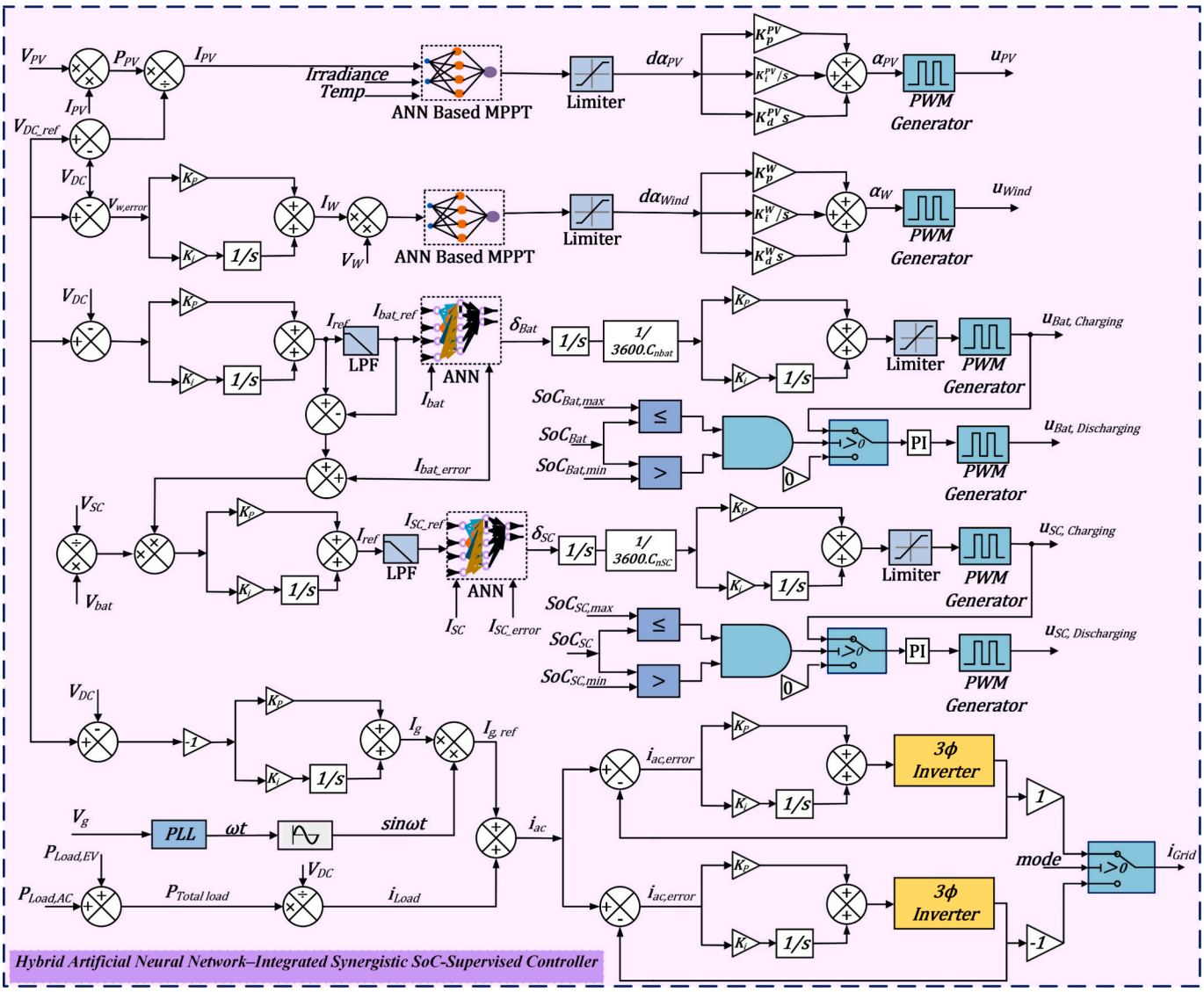

Fig. 11. Modeling of hybrid artificial neural network–integrated synergistic SoC-supervised controller (HANNI-S^3 Controller).

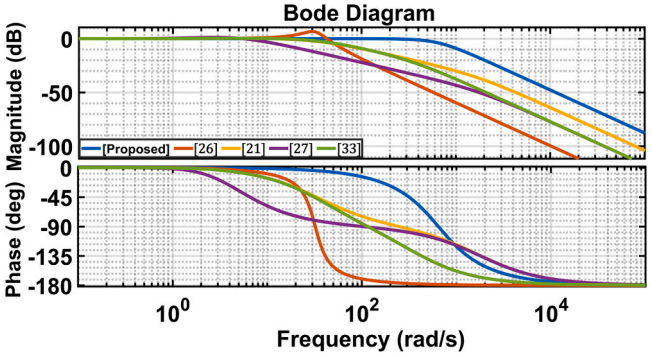

Fig. 12. Bode diagram comparing the proposed HANNI-S^3 controller with existing state-of-the-art controllers.

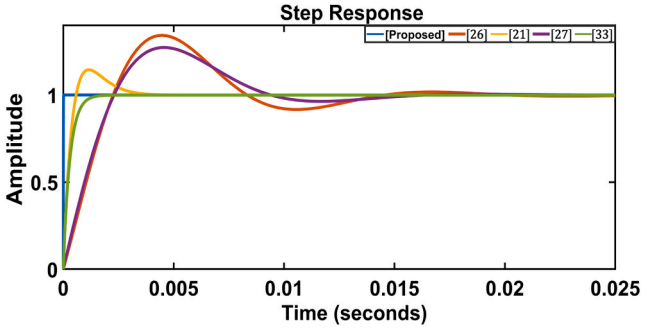

Fig. 13. Step response comparing the proposed HANNI-S^3 controller with existing state-of-the-art controllers.

($\zeta \approx 0.45 - 0.5$), leads to extended transient duration and elevated component stress, making these controllers unsuitable for applications requiring tight voltage regulation and smooth dynamic performance.

Together, these results confirm that the proposed HANNI-S^3 controller delivers the widest usable bandwidth, strongest high-frequency noise suppression, largest phase margin without gain peaking, and cleanest transient response, resulting in superior voltage regulation and minimal component stress under load disturbances.

4. Operational modes and energy management strategy algorithm for the hybrid grid connected MG system

The power management algorithm in Fig. 14 coordinates the real-time power flow among PV, wind, battery, SC, grid, and load components in a hybrid energy system. This proposed system operates under two primary power states: Excess Power Mode (EPM) and Deficit Power Mode (DPM). EPM is initiated when the total generated power $P_{GEN} > P_{PV} + P_{Wind}$ exceeds the load demand P_{Load}. During this state, excess energy is used to charge the battery and SC if their SoC is within allowable upper limits $(SOC_{Bat} > SOC_{Bat,max})$, $(SOC_{SC} > SOC_{SC,max})$; otherwise, the surplus power is exported to the grid. In this mode, the battery converter operates in buck mode, indicated by $Mode_{bat,ch} = 1$. On the other hand, DPM occurs when the generated power is insufficient $(P_{GEN} < P_{Load})$. The power deficit is met either by discharging the battery if $(SOC_{Bat} > SOC_{Bat,min})$ or by drawing power from the grid. In DPM, the converter operates in boost mode, with $Mode_{bat,disch} = 1$. Battery availability for operation is indicated by $Mode_{bat}$, which is set to 1 if within SoC limits, otherwise 0. Similarly, $Mode_{SC,ch}$ and $Mode_{SC,disch}$ are set to 1 when the SC is available for charging and discharging, respectively. This logic guarantees that power is distributed appropriately, the battery is protected from overcharging and there is a smooth exchange between renewable power, storage and the grid.

Considering all possible value combinations of the parameters, there are fifteen cases that one can deal with, as shown in Table 3, which contains conditions on power and SoC along with their respective mode's settings. All cases are discussed in detail below:

Case 1: $P_{PV+Wind} > P_{Load}$, $SOC_{Bat} < SOC_{Bat,max}$, $SOC_{SC,min} < SOC_{SC} > SOC_{SC,max}$

In this case, the total generated power from PV and wind is greater than the load demand (Mode = 0), and the battery's state of charge is lower than the maximum threshold ($Mode_{bat,ch} = 1$), which allows it to charge the battery. Meanwhile, the SC SoC lies between its minimum and maximum limits, so it is available for charging ($Mode_{SC,disch} = 1$). As a result, the SC supports the load by handling high-frequency transients while the battery charges with the excess available power. Since the battery is not fully charged and the generated power surpasses the load, no power is transmitted to the grid, and the grid current is zero, $i_g = 0$.

Case 2: $P_{PV+Wind+Bat} > P_{Load}$, $SOC_{Bat} > SOC_{Bat,min}$, $SOC_{SC,min} < SOC_{SC} > SOC_{SC,max}$

The total power generated from PV, wind, and battery sources exceeds the load demand, and thus the surplus energy is available for storage device (Mode = 1). The battery has sufficient SoC above its minimum threshold, allowing it to be discharged ($Mode_{bat,disch} = 1$). Meanwhile, the SC SoC is also above its minimum limit, enabling it to assist in absorbing high-frequency power components ($Mode_{SC,disch} = 1$). The grid remains idle in this condition, resulting in zero grid current, $i_g = 0$.

Case 3: $P_{Wind+Bat} > P_{Load}$, $P_{PV} = 0$, $SOC_{Bat} > SOC_{Bat,min}$, $SOC_{SC,min} < SOC_{SC} > SOC_{SC,max}$

The combined power from wind and battery sources exceeds the load power, fulfilling the demand without PV contribution (Mode = 1). The battery has adequate SoC and is available for discharging ($Mode_{bat,disch} = 1$). The SC is also within its operational SoC range and thus remains active in discharging mode to handle transient and high-frequency power ($Mode_{SC,disch} = 1$). As all power demands are met locally, the grid current is zero, $i_g = 0$.

Case 4: $P_{PV+Bat} > P_{Load}$, $P_{Wind} = 0$, $SOC_{Bat} > SOC_{Bat,min}$, $SOC_{SC,min} < SOC_{SC} > SOC_{SC,max}$

The PV and battery collectively supply more power than required by the load, enabling energy surplus management (Mode = 1). The battery is above its minimum SoC and actively discharges ($Mode_{bat,disch} = 1$). The SC, having sufficient SoC, assists by discharging to smooth out the power fluctuations ($Mode_{SC,disch} = 1$). No interaction with the grid occurs, resulting in zero grid current, $i_g = 0$.

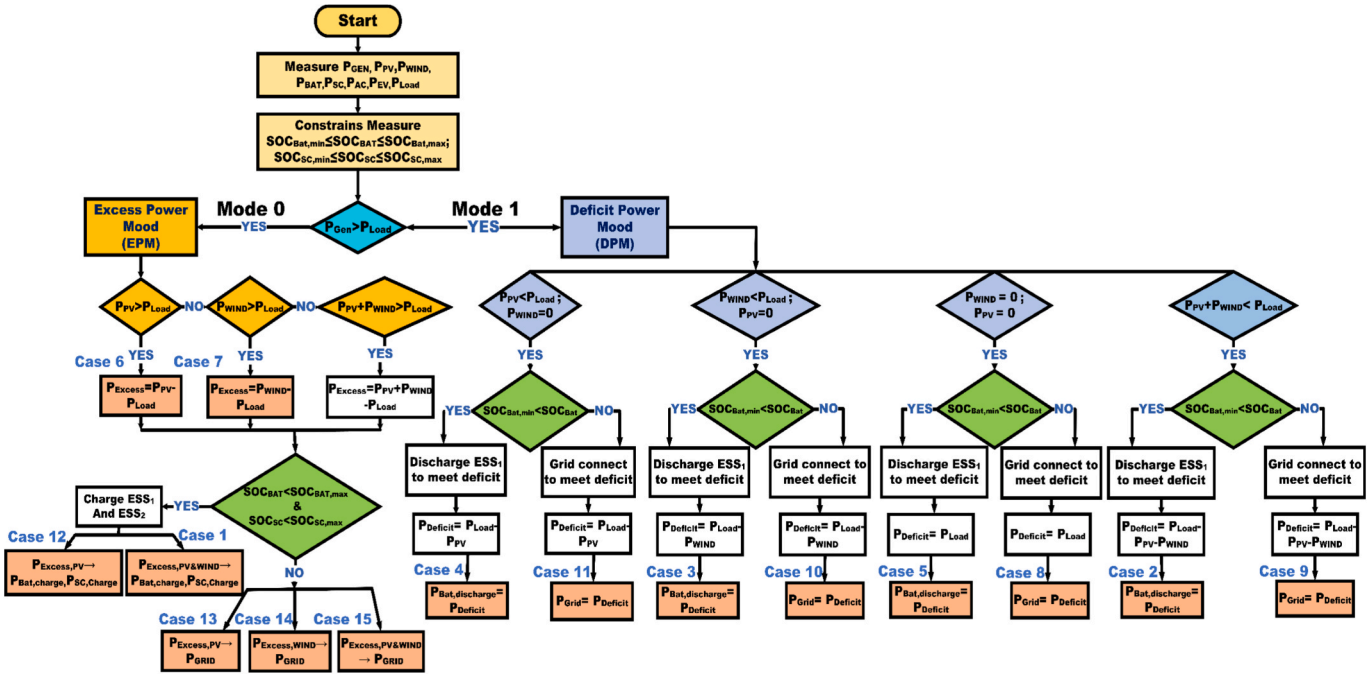

Fig. 14. Flowchart of the energy management strategy algorithm of the proposed system.

Table 3
Table of all possible cases with their corresponding modes:

Case	Conditions	Mode's setting
1	$P_{PV+Wind} > P_{Load}$ $SOC_{Bat} < SOC_{Bat,max}$ $SOC_{SC,min} < SOC_{SC} > SOC_{SC,max}$	$Mode = 0$ $Mode_{bat} = 1$ $Mode_{grid} = 0$ $Mode_{bat,ch} = 1$ $Mode_{SC,ch} = 1$
2	$P_{PV+Wind+Bat} > P_{Load}$ $SOC_{Bat} > SOC_{Bat,min}$ $SOC_{SC} > SOC_{SC,min}$	$Mode = 1$ $Mode_{bat} = 1$ $Mode_{grid} = 0$ $Mode_{bat,disch} = 1$ $Mode_{SC,disch} = 1$
3	$P_{Wind+Bat} > P_{Load}$ $SOC_{Bat} > SOC_{Bat,min}$ $SOC_{SC} > SOC_{SC,min}$	$Mode = 1$ $Mode_{bat} = 1$ $Mode_{grid} = 0$ $Mode_{bat,disch} = 1$ $Mode_{SC,disch} = 1$
4	$P_{PV+Bat} > P_{Load}$ $SOC_{Bat} > SOC_{Bat,min}$ $SOC_{SC} > SOC_{SC,min}$	$Mode = 1$ $Mode_{bat} = 1$ $Mode_{grid} = 0$ $Mode_{bat,disch} = 1$ $Mode_{SC,disch} = 1$
5	$P_{Bat} > P_{Load}$; $P_{PV} \& P_{Wind} = 0$ $SOC_{Bat} > SOC_{Bat,min}$ $SOC_{SC} > SOC_{SC,min}$	$Mode = 1$ $Mode_{bat} = 1$ $Mode_{grid} = 0$ $Mode_{bat,disch} = 1$ $Mode_{SC,disch} = 1$
6	$P_{PV} > P_{Load}$; $P_{Wind} = 0$ $SOC_{Bat} < SOC_{Bat,min}$ $SOC_{SC} > SOC_{SC,min}$	$Mode = 0$ $Mode_{bat} = 0$ $Mode_{grid} = 0$ $Mode_{SC,disch} = 1$
7	$P_{Wind} > P_{Load}$; $P_{PV} = 0$ $SOC_{Bat} < SOC_{Bat,min}$ $SOC_{SC} > SOC_{SC,min}$	$Mode = 0$ $Mode_{bat} = 0$ $Mode_{grid} = 0$ $Mode_{SC,disch} = 1$
8	$P_{Grid} > P_{Load}$; $P_{PV} \& P_{Wind} = 0$ $SOC_{Bat} < SOC_{Bat,min}$ $SOC_{SC} > SOC_{SC,min}$	$Mode = 1$ $Mode_{bat} = 0$ $Mode_{grid} = 1$ $Mode_{SC,disch} = 1$
9	$P_{PV+Wind+Grid} > P_{Load}$ $SOC_{Bat} \leq SOC_{Bat,min}$ $SOC_{SC} > SOC_{SC,min}$	$Mode = 1$ $Mode_{bat} = 1$ $Mode_{grid} = 1$ $Mode_{bat,ch} = 1$ $Mode_{SC,ch} = 1$
10	$P_{Wind+Grid} > P_{Load}$; $P_{PV} = 0$ $SOC_{Bat} \leq SOC_{Bat,min}$ $SOC_{SC} > SOC_{SC,min}$	$Mode = 1$ $Mode_{bat} = 1$ $Mode_{grid} = 1$ $Mode_{bat,ch} = 1$ $Mode_{SC,disch} = 1$
11	$P_{PV+Grid} > P_{Load}$; $P_{Wind} = 0$ $SOC_{Bat} \leq SOC_{Bat,min}$ $SOC_{SC} > SOC_{SC,min}$	$Mode = 1$ $Mode_{bat} = 1$ $Mode_{grid} = 1$ $Mode_{bat,ch} = 1$ $Mode_{SC,disch} = 1$
12	$P_{PV} > P_{Load}$ $SOC_{Bat} < SOC_{Bat,max}$ $SOC_{SC} > SOC_{SC,min}$	$Mode = 1$ $Mode_{bat} = 1$ $Mode_{grid} = 1$ $Mode_{bat,ch} = 1$ $Mode_{SC,disch} = 1$
13	$P_{PV} > P_{Load}$; $P_{PV} \rightarrow P_{Grid}$ $SOC_{Bat} \leq SOC_{Bat,max}$ $SOC_{SC} > SOC_{SC,min}$	$Mode = 0$ $Mode_{bat} = 0$ $Mode_{grid} = 1$ $Mode_{SC,disch} = 1$
14	$P_{PV+Wind} > P_{Load}$; $P_{PV\&Wind} \rightarrow P_{Grid}$ $SOC_{Bat} \leq SOC_{Bat,max}$ $SOC_{SC} > SOC_{SC,min}$	$Mode = 0$ $Mode_{bat} = 0$ $Mode_{grid} = 1$ $Mode_{SC,disch} = 1$
15	$P_{Wind} > P_{Load}$; $P_{Wind} \rightarrow P_{Grid}$ $SOC_{Bat} \leq SOC_{Bat,max}$ $SOC_{SC} > SOC_{SC,min}$	$Mode = 0$ $Mode_{bat} = 0$ $Mode_{grid} = 1$ $Mode_{SC,disch} = 1$

Case 5: $\mathbf{P_{Bat} > P_{Load}}$, $\mathbf{P_{PV}\&P_{Wind} = 0}$, $\mathbf{SOC_{Bat} > SOC_{Bat,min}}$, $\mathbf{SOC_{SC,min} < SOC_{SC} > SOC_{SC,max}}$

The battery alone is sufficient to power the load, as both PV and wind power sources are inactive (Mode = 1). Since the battery's SoC is above the minimum threshold, it discharges to supply the load ($Mode_{bat} = 1$ and $Mode_{bat,disch} = 1$). The SC also supports the transient load by discharging to cover dynamic components ($Mode_{SC,disch} = 1$). Grid current remains at zero, $i_g = 0$.

Case 6:$\mathbf{P_{PV} > P_{Load}, P_{Wind} = 0, SOC_{Bat} < SOC_{Bat,min}}$, $\mathbf{SOC_{SC,min} < SOC_{SC} > SOC_{SC,max}}$

PV power is sufficient to meet the load, but battery is below its minimum SoC thresholds and thus are not available for discharging (Mode = 0, $Mode_{bat} = 0$). The SC again supports the transient load by discharging to cover dynamic components ($Mode_{SC,disch} = 1$). The excess PV power cannot be stored, and the grid is used to balance the system, if needed. However, based on the mode settings, the grid current is considered zero here, $i_g = 0$.

Case 7: $\mathbf{P_{Wind} > P_{Load}}$, $\mathbf{P_{PV} = 0}$, $\mathbf{SOC_{Bat} < SOC_{Bat,min}}$, $\mathbf{SOC_{SC,min} < SOC_{SC} > SOC_{SC,max}}$

Only wind power is available and sufficient to supply the load (Mode = 0). The battery SoC is below the minimum level and thus inactive ($Mode_{bat} = 0$). However, the SC has sufficient SoC and is capable of discharging to address any rapid load variations ($Mode_{SC,disch} = 1$). Grid current is zero, $i_g = 0$.

Case 8:$\mathbf{P_{Grid} > P_{Load}, P_{PV}\&P_{Wind} = 0, SOC_{Bat} < SOC_{Bat,min}}$, $\mathbf{SOC_{SC} > SOC_{SC,min}}$

Here, the grid is the only power source, providing more energy than the load demands (Mode = 1). The battery is available for charging only ($Mode_{bat} = 0$). The SC is above the minimum SoC and is engaged in discharging to manage dynamic load requirements ($Mode_{SC,disch} = 1$). The presence of surplus grid power implies energy is being stored, and thus $i_g \neq 0$.

Case 9: $\mathbf{P_{PV+Wind+Grid} > P_{Load}}$, $\mathbf{SOC_{Bat} < SOC_{Bat,min}}$, $\mathbf{SOC_{SC} > SOC_{SC,min}}$

In this case, the load demand is met by the combined power from PV, wind, and grid (Mode = 1), as the battery's SoC has reached its minimum threshold ($Mode_{bat} = 1$, $Mode_{bat,ch} = 1$), making it available only for charging. The SC SoC is above its minimum limit, allowing it to discharge ($Mode_{SC,disch} = 1$). Therefore, the PV, wind, and Grid. The grid contributes to the load since the battery cannot store excess power, and the SC helps manage transient variations in load.

Case 10: $\mathbf{P_{Wind+Grid} > P_{Load}}$, $\mathbf{P_{PV} = 0}$, $\mathbf{SOC_{Bat} < SOC_{Bat,min}}$, $\mathbf{SOC_{SC} > SOC_{SC,min}}$

Here, only wind and Grid are supplying power (Mode = 1) because PV generation is zero. The battery is at or below its lower SoC limit ($Mode_{bat} = 1$, $Mode_{bat,ch} = 1$, $Mode_{bat,disch} = 0$), making it again only available for charging but can't discharge. The SC has enough charge to discharge ($Mode_{SC,disch} = 1$), and therefore helps support the transient load for a brief period. The system draws from the grid while the SC deals with high-frequency fluctuations due to its fast response characteristics.

Case 11: $\mathbf{P_{PV+Grid} > P_{Load}}$, $\mathbf{P_{Wind} = 0}$, $\mathbf{SOC_{Bat} < SOC_{Bat,min}}$, $\mathbf{SOC_{SC} > SOC_{SC,min}}$

In this scenario, the power is provided by PV and Grid (Mode = 1), with wind generation absent. The battery SoC is below its minimum threshold ($Mode_{bat} = 1$, $Mode_{bat,ch} = 1$), which preventing it from discharging. The SC has sufficient charge to discharge for transient load ($Mode_{SC,disch} = 1$). This configuration ensures continuity of supply while managing power fluctuations with the help of the SC.

Case 12: $\mathbf{P_{PV} > P_{Load}}$, $\mathbf{SOC_{Bat} > SOC_{Bat,max}}$, $\mathbf{SOC_{SC} > SOC_{SC,min}}$

In this case, PV generation alone exceeds the load (Mode = 1). The battery SoC is below its upper limit ($Mode_{bat} = 1$), allowing it to be charged ($Mode_{bat,ch} = 1$). The SC SoC is higher than its minimum threshold which allows it's to discharge ($Mode_{SC,disch} = 1$). This case ensures both energy storage devices charge using the surplus PV power. Grid power is not required, and grid current remains zero, $i_g = 0$.

Case 13: $\mathbf{P_{PV} > P_{Load}}$, $\mathbf{SOC_{Bat} < SOC_{Bat,max}}$, $\mathbf{P_{PV} \rightarrow P_{Grid}}$, $\mathbf{SOC_{SC} > SOC_{SC,min}}$

In this case, PV generation exceeds load demand, and the surplus power is transmitted to the grid (Mode = 0, $Mode_{grid} = 1$). As the battery SoC is at its maximum thus battery will not charge ($Mode_{bat,ch} = 0$), while the SC is able to discharge and supports load fluctuations ($Mode_{SC,disch} = 1$).

Case 14: $\mathbf{P_{PV+Wind} > P_{Load}}$, $\mathbf{SOC_{Bat} < SOC_{Bat,max}}$, $\mathbf{P_{PV\&Wind} \rightarrow P_{Grid}}$, $\mathbf{SOC_{SC} > SOC_{SC,min}}$

Here, both PV and wind provide more power than the load demand (Mode = 0), and the excess is transmitted to the grid. The battery is fully charged it is unavailable to absorb power and will remain disconnected ($Mode_{bat} = 0$). The SC is able to discharge ($Mode_{SC,disch} = 1$), managing fast transients for brief period.

Case 15: $\mathbf{P_{Wind} > P_{Load}}$, $\mathbf{SOC_{Bat} < SOC_{Bat,max}}$, $\mathbf{P_{Wind} \rightarrow P_{Grid}}$, $\mathbf{SOC_{SC} > SOC_{SC,min}}$

This case shows wind generation exceeding load demand (Mode = 0), with the excess sent to the grid. As the battery SoC is at its maximum thus battery will not charge ($Mode_{bat,ch} = 0$). The SC provides discharge support for transient load ($Mode_{SC,disch} = 1$). Similar to previous export scenarios, the system favors grid feed-in.

5. Results and discussion

The proposed Hybrid ANN-Integrated Synergistic SoC-Supervised Power Management System, shown in Fig. 1, is assessed using a grid-connected MG with dynamic loads. The simulations were conducted using MATLAB 2022a, with all models implemented in Simulink. The simulations used the Tustin/backward Euler solver with a fixed sample time of $1 \times 10^{-5} s$ to accurately capture fast transient dynamics. This system is tested over 15 cases divided into 4 scenarios that run over 8 s. The effectiveness and reliability of the proposed HANNI-S^3-PMS under the condition of rapid changes in the operating conditions is evaluated by different operation modes with different generation and load requirements.

5.1. Scenario 1: Optimal local energy utilization without grid support

From (0–2 s), Fig. 15(k) shows PV generated 4.35 kW, and the wind turbine supplied 2.55 kW. The load included 2.6 kW from EV and 2 kW from AC loads, totaling 4.6 kW. As generation exceeded demand, the grid was disconnected. The surplus power charged the battery, −2.3 kW and SC, −2.3 kW, with the SC managing the transient response. Between (2–4 s) PV output reduced to 2.2 kW, and wind power dropped to 1.95 kW. Meanwhile, AC load increased to 4 kW, and EV load decreased to 1.3 kW, resulting in a 5.3 kW total load. With available power at 4.15 kW, the 1.15 kW deficit was compensated by discharging the battery. And SC provided 1.15 kW at transient support to maintain system stability. In (4–6 s), PV was unavailable, and wind power declined to 1.35 kW. The AC load remained at 4 kW, and the EV load increased to 2.6 kW, making the total demand 6.6 kW. The battery discharged at 5.25 kW, and the SC contributed 4.1 kW at transient response, ensuring uninterrupted power through coordinated energy storage. The grid remained disconnected which resulting in grid current = 0 A. From (6–8 s) PV generation resumed at 3.25 kW, while the wind turbine was unavailable. The AC load dropped to 2 kW, and the EV load stayed at 2.6 kW. With lower demand, battery discharge reduced to 1.35 kW, and the SC absorbed −3.9 kW during transient stabilization. DC Bus voltage was maintained at 50 V as shown in Fig. 15(e). Inverter output was sinusoidal with 220.5 V RMS voltage; current varied with load at Fig. 15(f). Total Harmonic Distortion (THD) remained low: 0.53 % for voltage and 1.03 % for current, confirming high power quality in Fig. 15(i,j).

5.2. Scenario 2: Transitional management during generation drop and source recovery

From (0–2 s), Fig. 16(k) shows both PV and wind sources were unavailable. With an AC load of 2 kW and EV load of 2.6 kW, the battery discharged 4.6 kW, while the SC supplied an additional 4.6 kW to support transient stability. Between (2–4 s), PV system becomes active, delivering 6.65 kW, while the wind turbine remains inactive. Load demand rose to 6.6 kW where the AC load and EV load were 4 kW and 2.6 kW respectively. The battery's SoC approached its threshold limit and was subsequently disconnected due to low energy availability. Nevertheless, the SC discharged 6.65 kW to ensure transient support at this time. In (4–6 s), PV generation stopped, and the wind turbine produced 3.35 kW. The load dropped to 3.3 kW. The battery remained inactive due to insufficient power. The SC supplied 3.35 kW, maintaining system stability under transient conditions. From (6–8 s), renewable sources were unavailable, and the battery remained inactive. Load demand peaked at 6.6 kW. To meet the power deficit, the system draws 6.6 kW from the grid. During transient situations, the SC added 6.66 kW to stabilize the voltage in the system. In addition, the DC bus voltage was held constant at 50 V during the simulation as displayed in Fig. 16(e). The inverter output exhibited stable sinusoidal voltage (220.5 V RMS) and load-dependent current in Fig. 16(f). THD remained low: 0.57 % for voltage and 1.02 % for current, well within limits demonstrated in Fig. 16(i,j), confirming high power quality.

5.3. Scenario 3: Grid support activation during renewable and storage limitations

From (0–2 s), Fig. 17(k) shows PV and wind systems supplied 2.2 kW and 1.25 W, respectively, while load demand was total 4.6 kW, where the AC and EV loads were 2 kW and 2.6 kW, respectively. The resulting

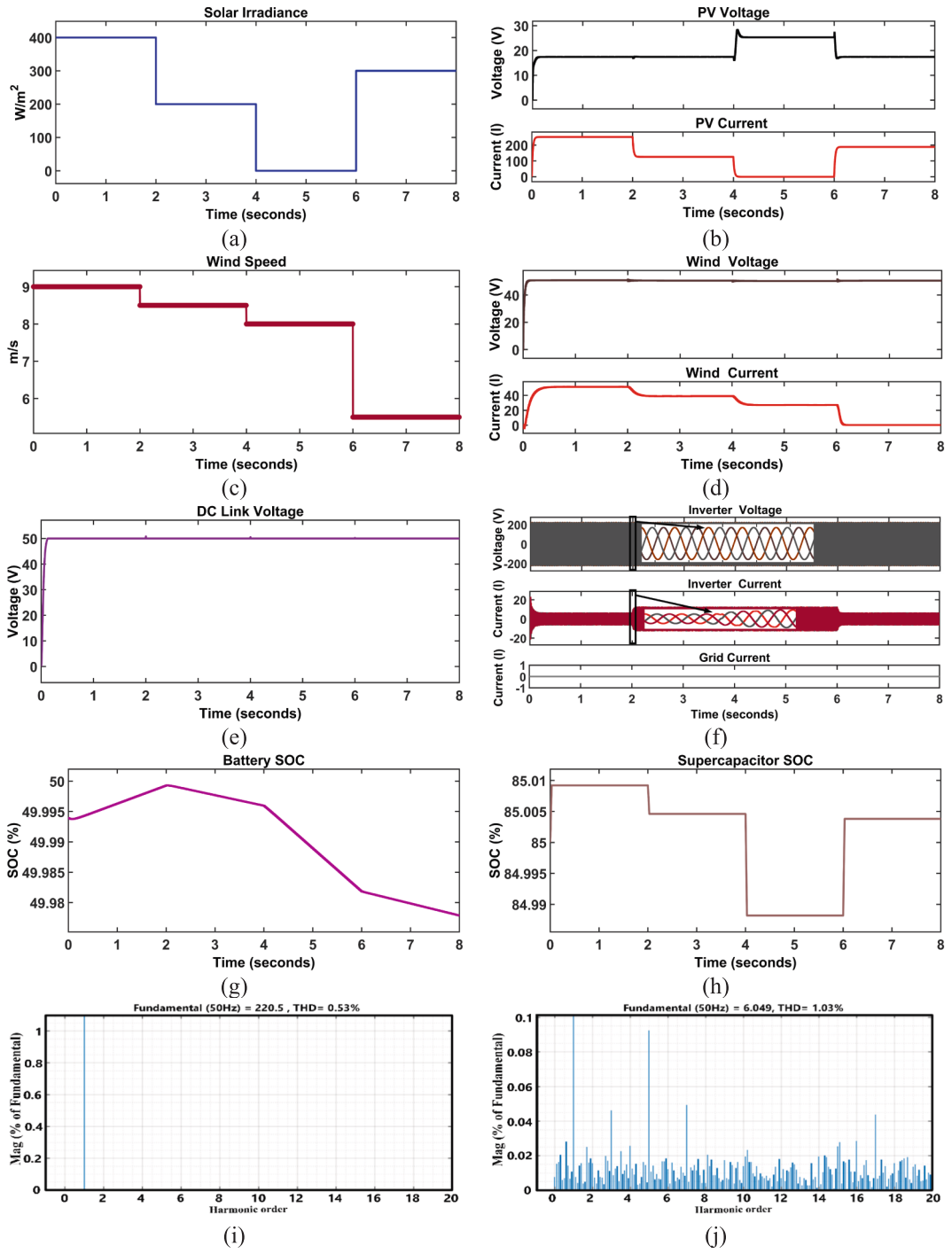

Fig. 15. (a) Solar irradiation, (b) PV voltage and current, (c) Wind speed, (d) Wind voltage and current, (e) DC link voltage, (f) Inverter voltage, Inverter current and Grid current (g) Battery SoC, (h) SC SoC, (i, j) THD of inverter's output voltage and current, (k) Power management profile.

generation shortfall required the grid to supply 4.6 kW. With the battery at its minimum SoC limit, thus it could not contribute and −3.45 kW power was used to charge the battery, and the SC absorbed −3.45 kW during transient stabilization. Between (2–4 s), only the wind system remained active, generating 0.7 kW, while load demand was 3.3 kW. The grid supplied 3.3 kW, and the SC discharged 2.75 kW briefly to support system transitions and ensure voltage stability. Between (4–8 s), PV generation resumed with 2.2 kW from (4–6 s) and increased to 3.3 kW at (6–8 s). Load remained constant at 6.6 kW. The grid compensated the deficit with 6.6 kW. The SC managed transients, absorbing −1.5 kW at (4–6 s) and −1.1 kW at (6–8 s). DC bus voltage remained stable at 50 V, with only minor transient spikes shown in Fig. 17(e). Inverter output in Fig. 17(f) gave a smooth and sinusoidal shape to both the voltage and the current curves. THD voltage was 0.58 % and THD current was 0.81 % as shown in Fig. 17(i,j), which are much below the acceptable limits and result in high power quality.

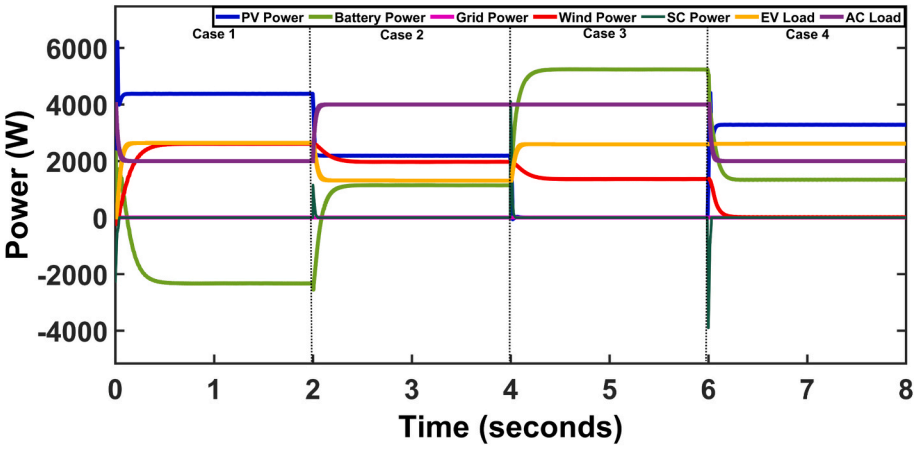

(k)

Fig. 15. (*continued*).

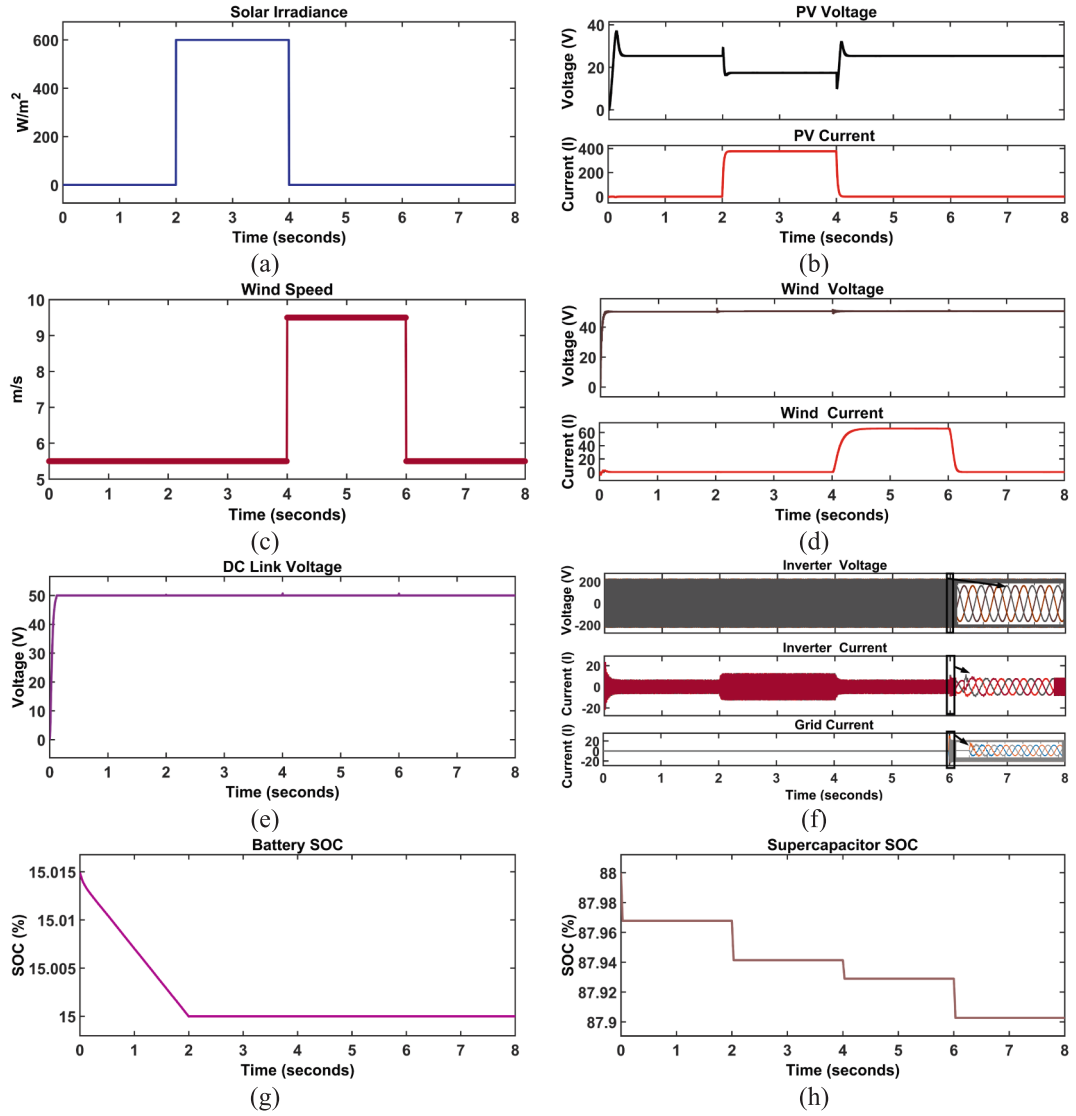

Fig. 16. (a) Solar irradiation, (b) PV voltage and current, (c) Wind speed, (d) Wind voltage and current, (e) DC link voltage, (f) Inverter voltage, Inverter current and Grid current (g) Battery SoC, (h) SC SoC, (i, j) THD of inverter's output voltage and current, (k) Power management profile.

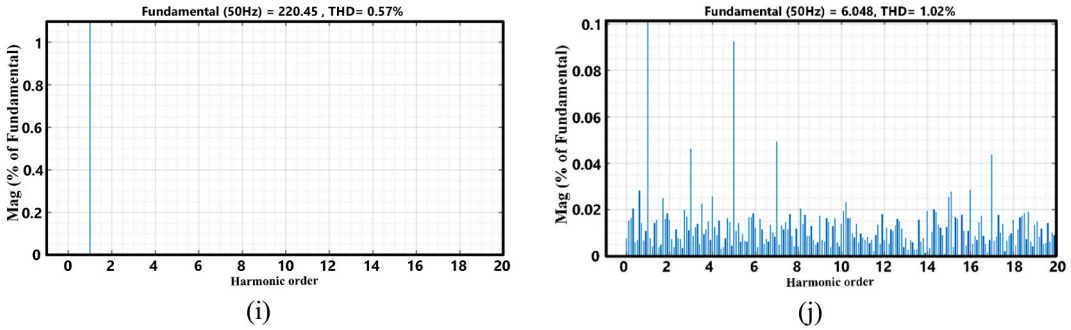

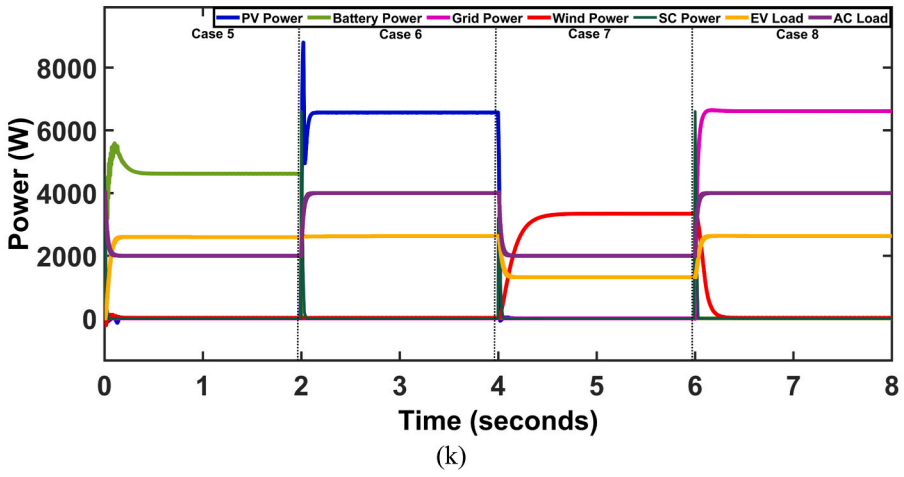

Fig. 16. (*continued*).

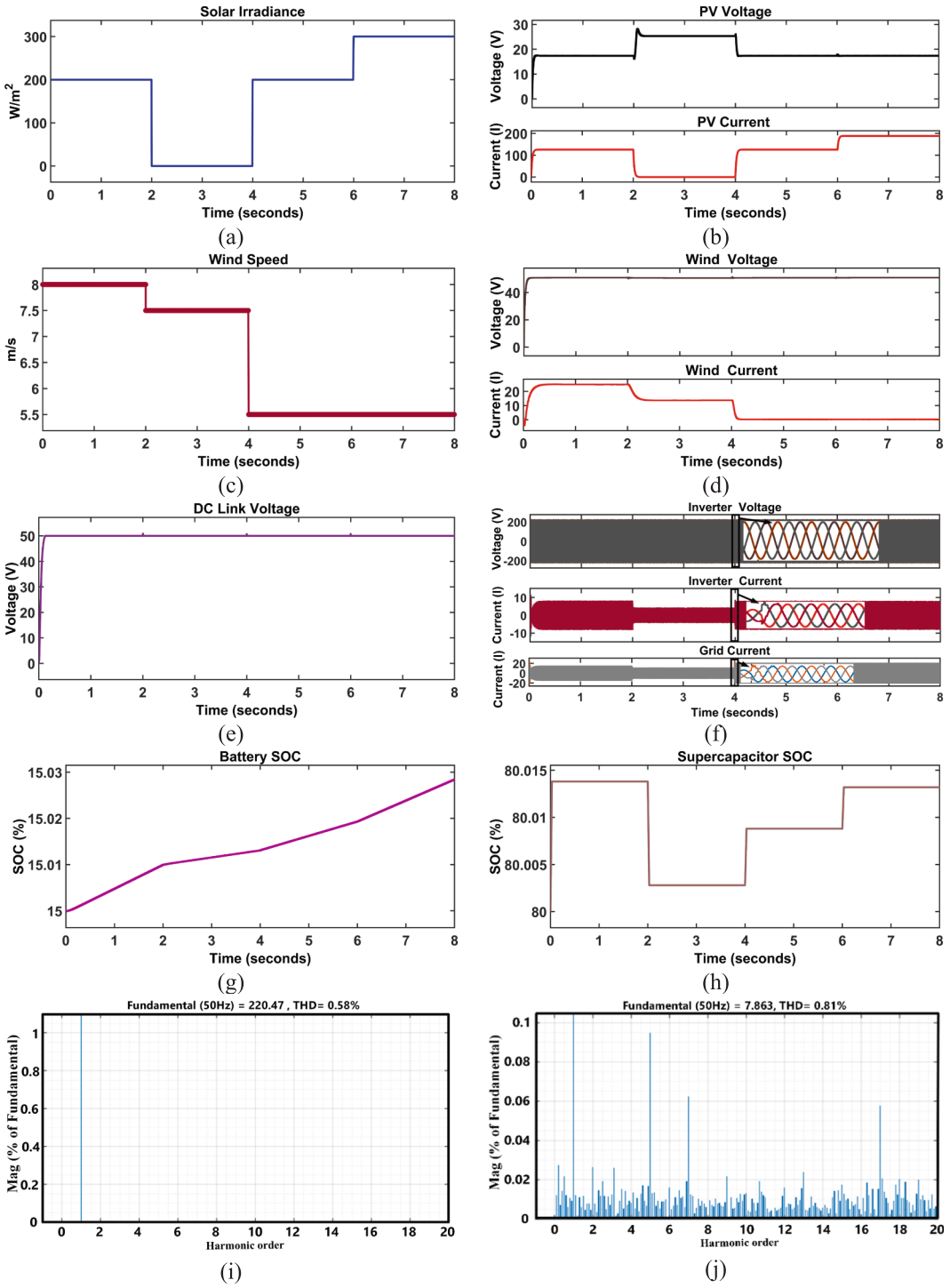

Fig. 17. (a) Solar irradiation, (b) PV voltage and current, (c) Wind speed, (d) Wind voltage and current, (e) DC link voltage, (f) Inverter voltage, Inverter current and Grid current (g) Battery SoC, (h) SC SoC, (i, j) THD of inverter's output voltage and current, (k) Power management profile.

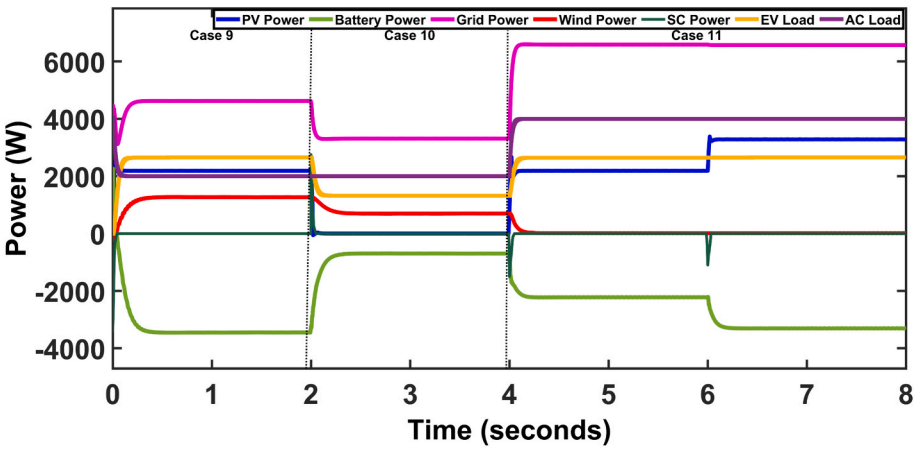

(k)

Fig. 17. (*continued*).

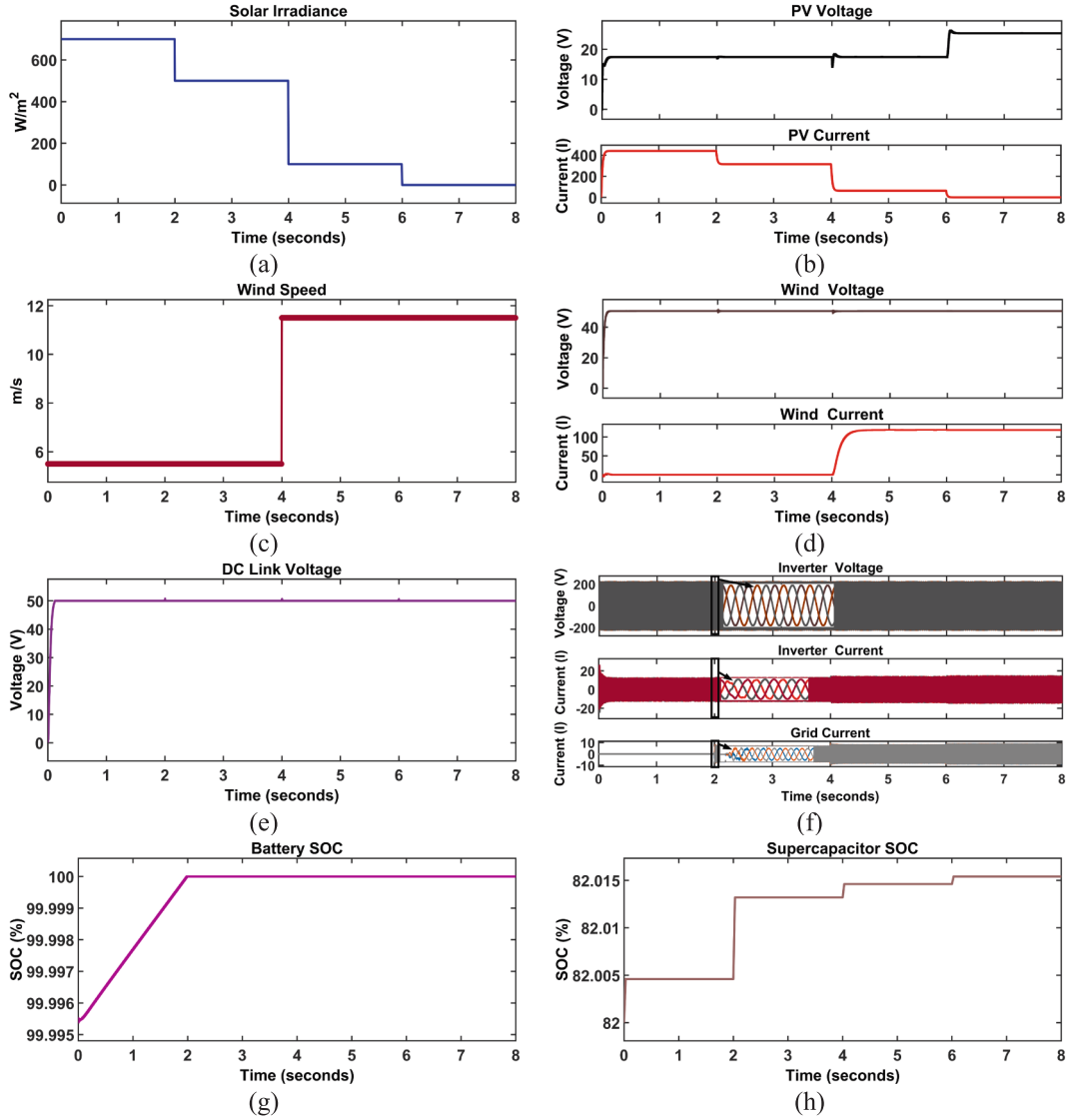

Fig. 18. (a) Solar irradiation, (b) PV voltage and current, (c) Wind speed, (d) Wind voltage and current, (e) DC link voltage, (f) Inverter voltage, Inverter current and Grid current (g) Battery SoC, (h) SC SoC, (i, j) THD of inverter's output voltage and current, (k) Power management profile.

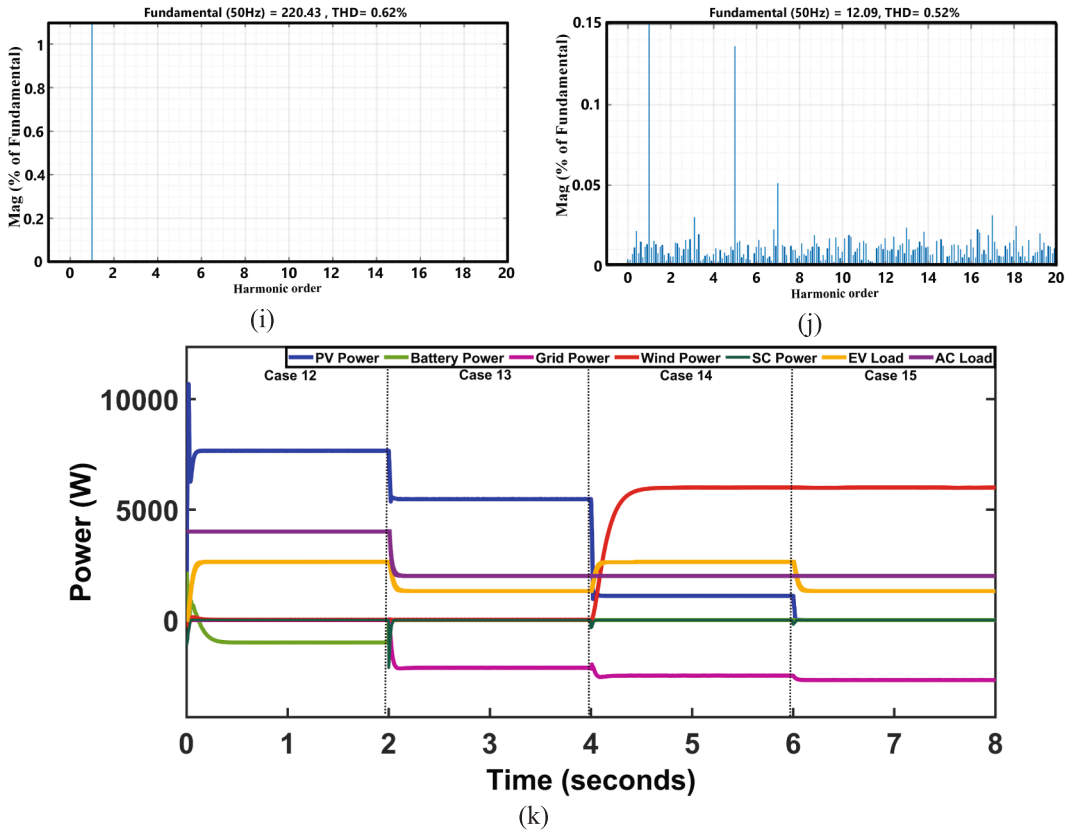

Fig. 18. (*continued*).

Table 4
Comparison between proposed HANNI-S^3-PMS and existing MG systems:

Ref. & Authors	Renewable Source Diversity	DC Link Voltage Regulation	Dynamic load capability	EV charger integrated	Grid Interaction
Maria C. Argyrou et al. (2021)	Absent	± 0.625 %	Unavailable	No	Interactive
Kuldeep Kumar and Sungwoo Bae (2022)	Absent	± 4 %	Unavailable	No	Interactive
Chandrakant L. Bhattar et al. (2023)	Absent	± 4 %	Unavailable	No	Interactive
Suchismita Patel et al. (2023)	Present	±4.2 %	Available	No	Stand-alone
Hassan Abouobaida et al. (2023)	Present	±0.25 %	Unavailable	No	Stand-alone
Ujjal Manandhar et al. (2019)	Absent	±2.9 %	Unavailable	No	Interactive
Proposed system	Present	± 1.76 %	Available	Yes	Interactive

5.4. Scenario 4: Power surplus management and export in grid-connected mode

From (0–2 s), Fig. 18(k) shows PV supplied 7.65 kW, with no wind generation. Load demand was 6.6 kW. The excess 1.05 KW was used to charge the battery, and the SC absorbed −1.05 kW during the transient response. Between (2–4 s), PV generation dropped to 5.45 kW, while load demand decreased to 3.3 kW. With the battery SoC at its maximum SoC limit, the surplus 2.15 kW was exported to the grid, and the SC absorbed −2.15 kW to maintain transient stability. At (4–6 s), wind generation supplied 6 kW, while PV generation reduced to 1.1 kW. The total load demand was 4.6 kW. Excess 2.5 kW was supplied into the grid, with the SC absorbed −.35 kW during transients. Between (6–8 s) wind power remained at 6 kW, while PV was inactive. The total load was 3.3 kW (AC made up 2 kW and EV made up 1.3 kW). Because the battery was fully charged, it provided the remaining 2.7 kW to the grid. SC absorbed −0.2 kW briefly to support system transitions. DC-link voltage was consistently held at 50 V demonstrated in Fig. 18(e), demonstrating strong voltage regulation. Inverter output and grid current showed clean sinusoidal waveforms shown in Fig. 18(f), indicating robust operation. THD values for voltage and current were 0.62 % and 0.52 %, respectively shown in Fig. 18(i,j), remaining well within standards, confirming high power quality and system reliability.

Table 5
Performance comparison of the proposed controller and conventional control methods.

Ref.	[21]	[24]	[26]	[32]	Proposed
Voltage regulation (V_{Reg})	± 2 V	± 1.92 V	± 2.5 V	± 2.72 V	± 0.88 V
Maximum peak overshoot (MP_{OS})	4 %	2 %	8 %	3.4 %	1.76 %
Settling time (t_{ss})	25 ms	30 ms	40 ms	440 ms	10 ms

6. Comparative analysis

6.1. Comparison of the proposed system with the existing studies

In this section, Table 4 compares the proposed system with existing studies in terms of renewable source diversity, voltage regulation, dynamic load capability, EV integration, and grid interaction. The

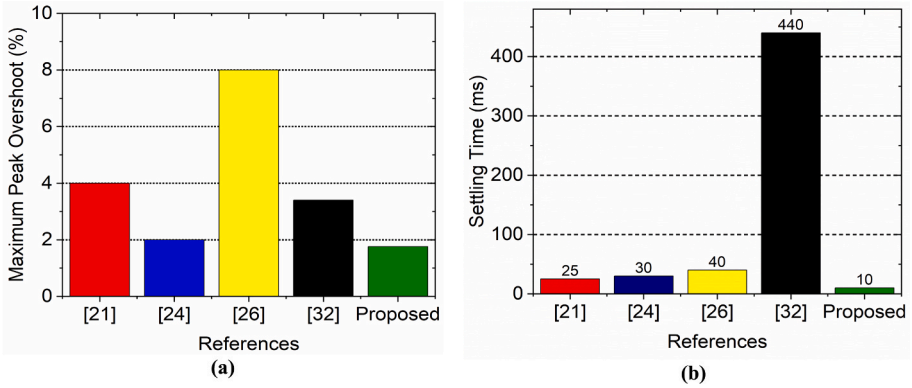

Fig. 19. Performance comparison of (a) maximum peak overshoot and (b) settling time for proposed and conventional power management strategies.

proposed method demonstrates enhanced performance and more comprehensive feature integration.

6.2. Performance comparison between proposed power management and conventional power management strategy

Table 5 and Fig. 19 presents a quantitative comparison between the proposed HANNI-S^3 Controller and conventional power management strategies. The focus of the analysis is mainly on three important performance measures: voltage regulation (V_{Reg}), maximum overshoot (MP_{OS}), and settling time (t_{ss}). These are critical for assessing the effectiveness and dynamic stability of power management algorithms in HESs.

Analysis was performed on bus voltage deviations under varying generation and load conditions to obtain values of the metrics that are relevant to the real-world operation behavior. The evaluation highlights voltage tracking capability, response speed, and recovery behavior during transient events. As shown in Table 5, the HANNI-S^3 Controller provides better voltage regulation, less peak overshoot, and quicker settling than the conventional power management techniques, which offer more consistent and efficient operation of the system.

7. Conclusion

This study presented HANNI-S^3-PMS as a comprehensive solution to the challenges of renewable intermittency, fast transients, and storage degradation in HMGs. The structure integrates solar PV, wind generation, battery-SC storage system, grid support and EV charging within one intelligent control strategy. The proposed hierarchical design combines fast PI regulation, ANN-based MPPT and power sharing, and a SoC-supervised layer with PLL synchronization. Thus, enabling seamless transitions between grid-connected and islanded modes. The extensive validation across various load patterns, renewable ramps and grid contingencies showed that HANNI-S^3-PMS can effectively capture the maximum share of renewable resources with a well-regulated DC-bus, rapid recovery from disturbances, efficient dynamic load balancing and decreased dependence on the grid along with reduced battery stress. These results show that HANNI-S^3-PMS delivers high adaptability, stability, and computational efficiency without relying on heavy optimizers or pre-tuned parameters, offering a scalable, data-driven solution for next-generation smart MGs.

Despite these promising results, some limitations remain. Such as the validation was done under simulation conditions, so, hardware-level uncertainties along with communications delay and long-term degradation effects were still to be considered. In addition, though ANN-based controllers produced excellent performance for the considered cases, their behavior during faults or scaling up the system is still to be investigated.

Future work will address these challenges through hardware-in-the-loop testing, edge computing deployment, and predictive deep-learning control to manage weather uncertainty, load variability, and user behavior. Extending the framework to coordinate multiple HANNI-S^3-PMS units across interconnected MGs and implementing market-based optimization will further enable peer-to-peer energy trading and active participation in grid services.

CRediT authorship contribution statement

Md. Badoruzzaman: Writing – original draft, Visualization, Validation, Software, Methodology, Investigation, Formal analysis, Data curation, Conceptualization. **Jahidul Islam Shuvo:** Writing – original draft, Visualization, Validation, Software, Resources, Methodology, Investigation, Formal analysis, Data curation, Conceptualization. **Shaikh Tawhidul Islam Anik:** Writing – original draft, Visualization, Software, Methodology, Investigation, Formal analysis, Conceptualization. **Shameem Ahmad:** Writing – review & editing, Writing – original draft, Validation, Supervision, Software, Resources, Project administration, Methodology, Investigation, Formal analysis. **A.S. Nazmul Huda:** Writing – review & editing, Validation, Supervision, Resources, Investigation. **Tofael Ahmed:** Writing – review & editing, Visualization, Validation, Software, Investigation. **Mazaher Karimi:** Writing – review & editing, Validation, Supervision, Project administration, Investigation, Funding acquisition.

Declaration of competing interest

The authors declare that they have no known competing financial interests or personal relationships that could have appeared to influence the work reported in this paper.

Acknowledgement

The research presented in the paper was develop within the project “Best4Grid – Vehicle battery storage for green transport and grid stability in the Nordics”, which is part of the Nordic Grand Solutions Programme funded by Nordic Energy Research.

Data availability

No data was used for the research described in the article.

References

[1] Mannan M, Mansor M, Reza MS, Roslan MF, Ker PJ, Hannan MA. Recent development of grid-connected microgrid scheduling controllers for sustainable energy: a bibliometric analysis and future directions. IEEE Access 2024;12: 90606–28. https://doi.org/10.1109/ACCESS.2024.3419443.
[2] Yuvaraj T, Thirumalai M, Dharmalingam M, Thanikanti SB, Padmanaban S. Smart energy management for revenue optimization and grid independence in an Indian

RDS. In: Energy Convers Manage: X, 26; 2025. https://doi.org/10.1016/j.ecmx.2025.100955. ISSN 2590-1745.
[3] Wallsgrove R, Woo J, Lee J-H, Akiba L. The emerging potential of microgrids in the transition to 100% renewable energy systems. Energies 2021;14:1687. https://doi.org/10.3390/en14061687.
[4] Krishnamurthy Senthil, Adewuyi Oludamilare Bode, Luwaca Emmanuel, Ratshitanga Mukovhe, Moodley Prathaban. Artificial intelligence-based forecasting models for integrated energy system management planning: An exploration of the prospects for South Africa2. Energy Convers Manage: X 2024;24:10077. https://doi.org/10.1016/j.ecmx.2024.100772. ISSN 2590-1745.
[5] Zolfaghari Mahdi, Gharehpetian Gevork B, Shafie-khah Miadreza, Catalão João PS. Comprehensive review on the strategies for controlling the interconnection of AC and DC microgrids. Int J Elect Power Energy Syst 2022;136:107742. https://doi.org/10.1016/j.ijepes.2021.107742. ISSN 0142-0615.
[6] Falope T, Lao L, Hanak D, Huo Da. Hybrid energy system integration and management for solar energy: a review. Energy Convers Manage: X 2024;21:100527. https://doi.org/10.1016/j.ecmx.2024.100527. ISSN 2590-1745.
[7] Bortolini Marco, Gamberi Mauro, Graziani Alessandro. Technical and economic design of photovoltaic and battery energy storage system. Energy Convers Manage 2014;86:81–92. https://doi.org/10.1016/j.enconman.2014.04.089. ISSN 0196-8904.
[8] Abbasi AR, Baleanu D. Recent developments of energy management strategies in microgrids: an updated and comprehensive review and classification. Energy Convers Manage 2023;297:117723. https://doi.org/10.1016/j.enconman.2023.117723. ISSN 0196-8904.
[9] Banghua Du, Zhu Shihao, Zhu Wenchao, Xinyu Lu, Li Yang, Xie Changjun, et al. Energy management and performance analysis of an off-grid integrated hydrogen energy utilization system. Energy Convers Manage 2024;299:117871. https://doi.org/10.1016/j.enconman.2023.117871. ISSN 0196-8904.
[10] Hajiaghasi Salman, Salemnia Ahmad, Hamzeh Mohsen. Hybrid energy storage system for microgrids applications: a review. J Energy Storage 2019;21:543–70. https://doi.org/10.1016/j.est.2018.12.017. ISSN 2352-152X.
[11] M. Badoruzzaman et al., "Autonomous Power and Dynamic Load Management in Grid-Connected Microgrid with Supercapacitor and EV Integration," 2025 International Conference on Electrical, Computer and Communication Engineering (ECCE), Chittagong, Bangladesh, 2025, pp. 1-6, doi: 10.1109/ECCE64574.2025.11013269.
[12] Faisal M, Hannan MA, Ker PJ, Hussain A, Mansor MB, Blaabjerg F. Review of energy storage system technologies in microgrid applications: issues and challenges. IEEE Access 2018;6:35143–64. https://doi.org/10.1109/ACCESS.2018.2841407.
[13] Abdelghany Muhammad Bakr, Mariani Valerio, Liuzza Davide, Glielmo Luigi. Hierarchical model predictive control for islanded and grid-connected microgrids with wind generation and hydrogen energy storage systems. Int J Hydrogen Energy 2024;51(Part D):595–610. https://doi.org/10.1016/j.ijhydene.2023.08.056. ISSN 0360-3199.
[14] Pannala S, Patari N, Srivastava AK, Padhy NP. Effective control and management scheme for isolated and grid connected DC microgrid. IEEE Trans Industry Appl Nov.-Dec. 2020;56(6):6767–80. https://doi.org/10.1109/TIA.2020.3015819.
[15] Dhifli M, Lashab A, Guerrero JM, Abusorrah A, Al-Turki YA, Cherif A. Enhanced intelligent energy management system for a renewable energy-based AC microgrid. Energies 2020;13:3268. https://doi.org/10.3390/en13123268.
[16] Aguila-Leon JC, Vargas-Salgado C, Chiñas-Palacios D, Díaz-Bello EM. Model for a standalone hybrid microgrid through a particle swarm optimization and artificial neural networks approach. Energy Convers Manage 2022;267:115920. https://doi.org/10.1016/j.enconman.2022.115920. ISSN 0196-8904.
[17] Bihari SP, et al. A comprehensive review of microgrid control mechanism and impact assessment for hybrid renewable energy integration. IEEE Access 2021;9:88942–58. https://doi.org/10.1109/ACCESS.2021.
[18] Morstyn T, Hredzak B, Agelidis VG. Control strategies for microgrids with distributed energy storage systems: an overview. IEEE Trans Smart Grid July 2018;9(4):3652–66. https://doi.org/10.1109/TSG.2016.2637958.
[19] Roy Kallol, Mandal Kamal Krishna, Mandal Atis Chandra, Patra Sankar Narayan. Analysis of energy management in micro grid – A hybrid BFOA and ANN approach. Renew Sustain Energy Rev 2018;82(Part 3):4296–308. https://doi.org/10.1016/j.rser.2017.07.037. ISSN 1364-0321.
[20] Argyrou MC, Marouchos CC, Kalogirou SA, Paul C. A novel power management algorithm for a residential grid-connected PV system with battery-supercapacitor storage for increased self-consumption and self-sufficiency. Energy Convers Manage 2021;246:114671. https://doi.org/10.1016/j.enconman.2021.114671. ISSN 0196-8904.
[21] Kumar Kuldeep, Bae Sungwoo. Dynamic power management based on model predictive control for hybrid-energy-storage-based grid-connected microgrids. Int J Elect Power Energy Syst 2022;143:108384. https://doi.org/10.1016/j.ijepes.2022.108384. ISSN 0142-0615.
[22] Kandari Ritu, Gupta Pankaj, Kumar Ashwani. Battery state of charge based improved adaptive droop control for power management of a microgrid having large scale renewable generation. Sustain Energy Technol Assess 2023;57:103146. https://doi.org/10.1016/j.seta.2023.103146. ISSN 2213-1388.
[23] Abouobaida Hassan, de Oliveira-Assis Lais, Soares-Ramos Emanuel PP, Mahmoudi Hassane, Guerrero Josep M, Jamil Mohsin. Energy management and control strategy of DC microgrid based hybrid storage system. Simul Model Pract Theory 2023;124:102726. https://doi.org/10.1016/j.simpat.2023.102726. ISSN 1569-190X.
[24] Bhattar CL, Chaudhari MA. Centralized energy management scheme for grid connected DC microgrid. IEEE Syst J Sept. 2023;17(3):3741–51. https://doi.org/10.1109/JSYST.2022.3231898.
[25] Farrokhi Ehsan, Ghoreishy Hoda, Ahangar Roya Ahmadi. Optimization-based power management for battery/supercapacitor hybrid energy storage system with load estimation capability in a DC microgrid. Int J Elect Power Energy Syst 2024;155(Part B):109665. https://doi.org/10.1016/j.ijepes.2023.109665. ISSN 0142-0615.
[26] Patel S, Ghosh A, Ray PK, Gurugubelli V. Effective power management strategy and control of a hybrid microgrid with hybrid energy storage systems. IEEE Trans Industry Appl Nov.-Dec. 2023;59(6):7341–55. https://doi.org/10.1109/TIA.2023.3303862.
[27] Patel Suchismita, Ghosh Arnab, Ray Pravat Kumar. Efficient power management and control of DC microgrid with supercapacitor-battery storage systems. J Energy Storage 2023;73(Part C):109082. https://doi.org/10.1016/j.est.2023.109082. ISSN 2352-152X.
[28] Soliman Mohamed S, Belkhier Youcef, Ullah Nasim, Achour Abdelyazid, Alharbi Yasser M, Alahmadi Ahmad Aziz Al, et al. Supervisory energy management of a hybrid battery/PV/tidal/wind sources integrated in DC-microgrid energy storage system. Energy Rep 2021;7:7728–40. https://doi.org/10.1016/j.egyr.2021.11.056. ISSN 2352-4847.
[29] Bai W, Sechilariu M, Locment F. DC microgrid system modeling and simulation based on a specific algorithm for grid-connected and islanded modes with real-time demand-side management optimization. Appl Sci 2020;10:2544. https://doi.org/10.3390/app10072544.
[30] Sandeep SD, Mohanty S. Artificial rabbits optimized neural network-based energy management system for PV, battery, and supercapacitor based isolated DC microgrid system. IEEE Access 2023;11:142411–32. https://doi.org/10.1109/ACCESS.2023.3340856.
[31] Kamel A, Rezk H, Shehata N, Thomas J. Energy Management of a DC Microgrid Composed of Photovoltaic/Fuel Cell/Battery/Supercapacitor Systems. Batteries 2019;5:63. https://doi.org/10.3390/batteries5030063.
[32] Manandhar U, et al. Energy management and control for grid connected hybrid energy storage system under different operating modes. IEEE Trans Smart Grid March 2019;10(2):1626–36. https://doi.org/10.1109/TSG.2017.2773643.
[33] Shuvo Jahidul Islam, Badoruzzaman Md, Anik Shaikh Tawhidul Islam, Ahmad Shameem, Ahmed Tofael, Karimi Mazaher. Hybrid energy storage power management system harnessing battery-supercapacitor synergy for grid-isolated DC microgrid. J Energy Storage 2025;119:116170. https://doi.org/10.1016/j.est.2025.116170. ISSN 2352-152X.
[34] Zhu H, Ahmed SAZ, Alfakih MA, Abdelbaky MA, Sayed AR, Saif MAA. Photovoltaic failure diagnosis using sequential probabilistic neural network model. IEEE Access 2020;8:220507–22. https://doi.org/10.1109/ACCESS.2020.3043129.
[35] Kumaraswamy M, Naik KA. Backpropagation artificial neural network-based maximum power point tracking controller with image encryption inspired solar photovoltaic array reconfiguration. Eng Appl Artif Intell 2024;136(Part A):108979. https://doi.org/10.1016/j.engappai.2024.108979. ISSN 0952-1976.
[36] Haq IU, Khan Q, Ullah S, Khan SA, Akmeliawati R, Khan MA, et al. Neural network-based adaptive global sliding mode MPPT controller design for stand-alone photovoltaic systems. PLoS ONE 2022;17(1):e0260480. https://doi.org/10.1371/journal.pone.0260480.
[37] van der Broeck CH, De Doncker RW, Richter SA, von Bloh J. Unified control of a buck converter for wide load range applications. 2014 IEEE Applied Power Electronics Conference and Exposition - APEC 2014, Fort Worth, TX, USA, 2014, pp. 2788-2795, doi: 10.1109/APEC.2014.6803699.
[38] Majout Btissam, Bossoufi Badre, Karim Mohammed, Skruch Paweł, Mobayen Saleh, El Mourabit Youness, El Zair Zakaria, Laggoun. Artificial neural network-based direct power control to enhance the performance of a PMSG-wind energy conversion system under real wind speed and parameter uncertainties: an experimental validation. Energy Rep 2024;11:4356–78. https://doi.org/10.1016/j.egyr.2024.03.039. ISSN 2352-4847.
[39] Singh Prashant, Lather Jagdeep Singh. Dynamic power management and control for low voltage DC microgrid with hybrid energy storage system using hybrid bat search algorithm and artificial neural network. J Energy Storage 2020;32:101974. https://doi.org/10.1016/j.est.2020.101974. ISSN 2352-152X.
[40] Zhu T, Wills RGA, Lot R, Ruan H, Jiang Z. Adaptive energy management of a battery-supercapacitor energy storage system for electric vehicles based on flexible perception and neural network fitting. Appl Energy 2021;292:116932. https://doi.org/10.1016/j.apenergy.2021.116932. ISSN 0306-2619.
[41] Argyrou Maria C, Marouchos Christos C, Kalogirou Soteris A, Christodoulides Paul. Modeling a residential grid-connected PV system with battery–supercapacitor storage: control design and stability analysis. Energy Rep 2021;7:4988–5002. https://doi.org/10.1016/j.egyr.2021.08.001. ISSN 2352-4847.